Chemical Engineering Journal 484 (2024) 149480

Contents lists available at ScienceDirect

Chemical Engineering Journal

journal homepage: www.elsevier.com/locate/cej

CFD-DEM modeling of dense gas-solid reacting flow in the framework of GPU

Jiahui Yu [a], Shuai Wang [a,*], Kun Luo [a,b,*], Jianren Fan [a,b]

[a] State Key Laboratory of Clean Energy Utilization, Zhejiang University, Hangzhou 310027, PR China
[b] Shanghai Institute for Advanced Study of Zhejiang University, Shanghai 200120, PR China

ARTICLE INFO

Keywords:
Heat and mass transfer
CFD-DEM
GPU
Numerical simulation
Gas-solid reacting flow

ABSTRACT

Dense gas–solid reacting flow widely exists in kinds of engineering fields, such as blast furnace ironmaking, pharmaceutical manufacturing, energy conversion, and chemical engineering. These processes containing both physical and chemical changes are extremely complex. Revealing the basic principles of the gas–solid flow government and thermochemical behavior is critical to the optimization, design, and control of kinds of dense gas–solid reacting systems. Computational fluid dynamics – discrete element method (CFD-DEM) is considered a potential tool to achieve this goal, which suffers from expensive computational resources. Accordingly, this work develops a graphics processing unit (GPU)-accelerated CFD-DEM reactive model, integrating with heat transfer, heterogeneous reactions, and homogenous reactions. The accuracy of the GPU-accelerated heat and mass transfer sub-models are detailly verified and the simulation results agree well with analytic solutions. Additionally, the current model can successfully simulate the thermochemical behavior of the particle cooling process and the coal-fueled chemical looping gasification process, confirming its reliability in numerically studying dense gas–solid reacting flow. Furthermore, the GPU-accelerated strategy is demonstrated to perform great speed-up performance and stability. This work provides a reliable and high-performance parallel calculation method for numerically studying dense gas–solid reacting flow.

1. Introduction

Dense gas–solid reacting flow exists in various engineering fields, such as blast furnace ironmaking, biomass gasification, coal combustion, and chemical looping combustion [1–5]. It commonly occurs in kinds of fluidized equipment, such as bubbling fluidized bed (BFB), dual circulating fluidized bed (DCFB), and fixed bed. The thermochemical conversion process of solid fuels involves complicated multi-physics processes such as hydrodynamics, heat transfer, homogenous reactions, and heterogeneous reactions [6–8]. Taking the biomass gasification process in a BFB for example, a series of hydrodynamics and thermochemical behavior take place simultaneously at different spatial scales [9], as shown in Fig. 1. Specifically, two types of bed materials are fluidized and undergo solid mixing and segregation. The dilute phase appears in the upper part and the dense emulsion phase can be observed in the lower part which is dominated by bubble evolution. The bed materials undergo intensive heat transfer because of the large heat capacity and the biomass particles experience drying, pyrolysis, and gasification processes with the increase in temperature. These complex processes bring a huge difficulty to an in-depth understanding of such complex systems. Therefore, it is of great importance to deepen the comprehensive understanding of the thermochemical and physical characteristics of dense gas–solid reacting systems.

Up to now, lots of experimental studies have been accomplished to preliminarily understand some basic principles of dense gas–solid reacting flow, such as pressure drop, temperature distribution, and gaseous product distribution [10–13]. Because of the limitation of the non-intrusive nature of measure devices and severe operating conditions, only a few macroscopic variables can be obtained by experimental measurements. Meanwhile, it is unable to obtain detailed gas–solid microscopic behavior, heat and mass transfer contribution, and associated reactions by experiment, which are essential for optimizing dense gas–solid reacting systems.

Due to the development of numerical computation and computer, computational fluid dynamics (CFD) has been considered as a cost-effective, repeatable, and powerful alternative tool to in-depth study dense gas–solid reacting systems. Based on a comprehensive review [14], the CFD methods are classified as the Eulerian-Eulerian (E-E)

* Corresponding authors at: State Key Laboratory of Clean Energy Utilization, Zhejiang University, Hangzhou 310027, PR China (K. Luo).
E-mail addresses: wshuai2014@zju.edu.cn (S. Wang), zjulk@zju.edu.cn (K. Luo).

https://doi.org/10.1016/j.cej.2024.149480
Received 22 November 2023; Received in revised form 20 January 2024; Accepted 6 February 2024
Available online 9 February 2024

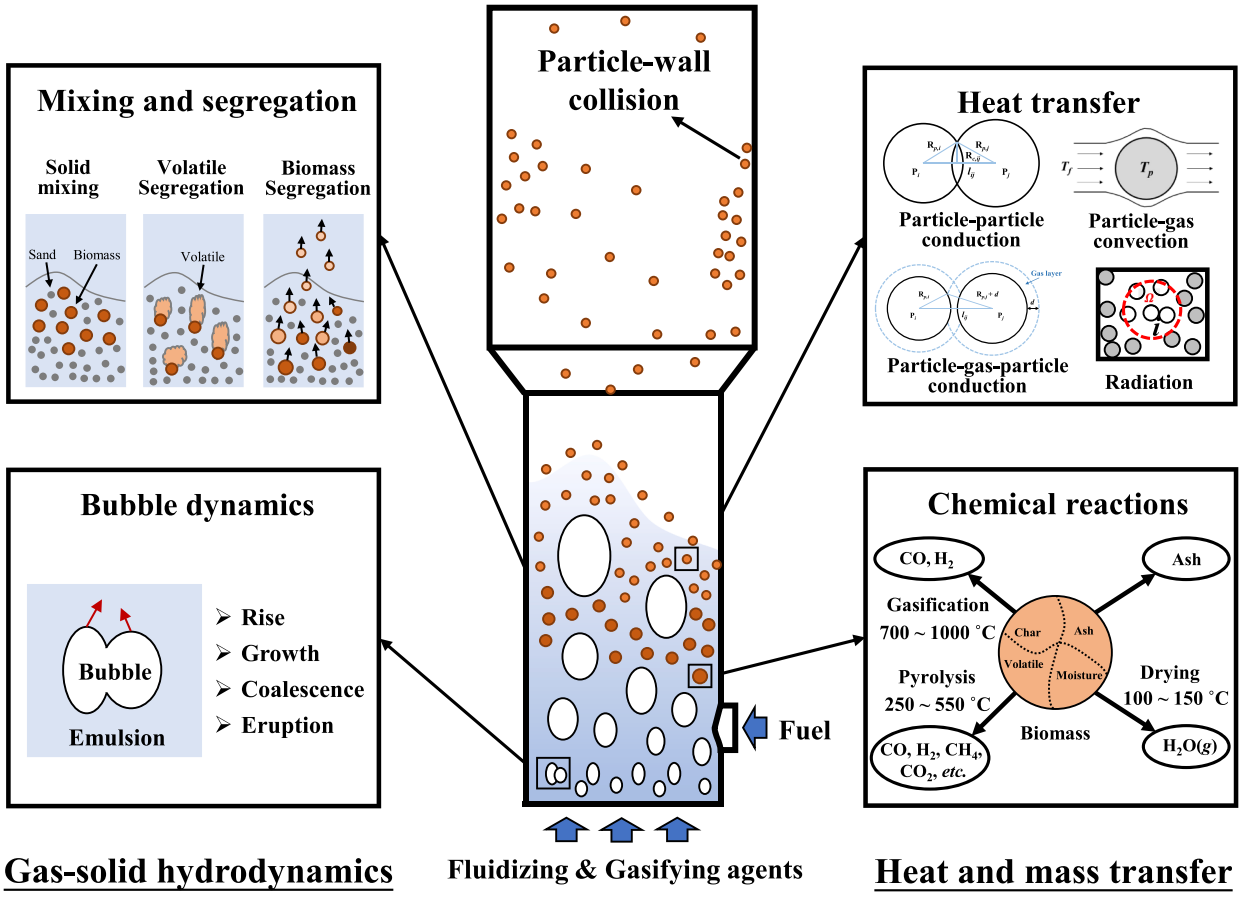

Fig. 1. Diagrammatical of multi-physics processes: biomass gasification process in a BFB gasifier.

framework and the Eulerian-Lagrangian (E-L) framework because of different treatments of the solid phase. The former considers the solid phase as the continuum and the kinetic theory of granular flows (KTGF) is adopted to solve the particle–particle collisions under the Eulerian framework. Due to the simplification of the particle phase, the E-E framework has been widely adopted for numerically studying various dense gas–solid reacting systems because of its strength of computational convenience [15,16]. However, it has the intrinsic limitation of failing to obtain detailed particle information. Comparably, the E-L framework can accurately describe the particle phase. As a representation, the computational fluid dynamics – discrete element method (CFD-DEM) can track each particle's movement and accurately solve the inter-particle collision, which can obtain abundant particle-scale information. Thus, the CFD-DEM method has been widely adopted to numerically study the multiphase flow and thermochemical behavior in fluidizing facilities due to the ability to be coupled with heat transfer sub-models, heterogeneous reactions, and homogenous reactions. Recently, Wang et al. [17] developed the CFD-DEM model coupled with thermochemical sub-models and particle-size polydispersity which showed great accuracy by validating the particle diameter, mixing index, and particle temperature. The thermochemical behavior of char combustion was numerically studied. Kong et al. [18] numerically studied the biomass gasification process using the CFD-DEM method considering thermochemical and polydispersity effects. The particle scale information was thoroughly discussed with the investigation of some key operating parameters on particle behavior. In addition, the CFD-DEM method also has extensive applications such as blast furnace ironmaking, chemical looping combustion, additive manufacturing, and fluid catalytic cracking, underpinning reactor design and process optimization [19,20]. Unfortunately, the calculation of particle–particle collision needs huge computational resources, thus, the CFD-DEM method is limited to studying small-scale reactors.

In recent years, various speed-up strategies for the CFD-DEM method have been proposed with the development of numerical algorithms and computer hardware. Due to its highly parallel structure and large data throughput, the graphics processing unit (GPU) has been considered a promising tool among all speed-up strategies. Especially, great speed-up performance has been proven in the simulation of granular flow, in which the GPU has been utilized for parallel simulations with a huge number of particles. Recently, several researchers have attempted to develop the GPU-accelerated CFD-DEM method in multiphase flow. Lu et al. [21] developed a GPU-accelerated DEM code coupled with the CFD model to numerically study granular and gas–solid two-phase flow. The Fortran based CFD solver was coupled with the CUDA/C++ based DEM solver. Norouzi et al. [22] developed a new GPU-accelerated CFD-DEM method in which the CFD solver is based on the open-source CFD code and the DEM solver is based on their in-house DEM code. The new model was evaluated in three different cases of gas–solid two-phase flow and great acceleration performance can be obtained. However, the current studies only focus on the hydrodynamics without considering the thermochemical behavior, which limits its application in numerically studying gas–solid reacting flow systems. More attention should be paid to extending the existing solver to integrate with mass, momentum, energy, and species changes. Furthermore, the communication overhead between CPU and GPU is time-consuming and needs to be optimized.

To bridge this research gap, the current work develops a GPU-accelerated CFD-DEM reactive model, integrating with heat transfer, heterogeneous reactions, and homogenous reactions, which can accurately and efficiently simulate the hydrodynamics and thermochemical behavior in fluidizing facilities. To minimize the communication overhead between CPU and GPU, the pinned memory is adopted which can significantly reduce the time consumption of data transfer between CPU

and GPU. The structure of this work is: Section 2 gives the governing equations of gas and solid phase, heat transfer sub-models, and chemical reaction kinetics. Section 3 verifies the accuracy of the heat and mass transfer sub-models. Then the model is used to numerically study the particle cooling process and the coal-fueled chemical looping gasification process in Section 4. The speed-up performance of the GPU-accelerated CFD-DEM reactive model is illustrated in Section 5. Conclusions are summarized in Section 6.

2. Mathematical model

A GPU-accelerated CFD-DEM reactive model is developed for simulating dense gas–solid reacting flow. The gas phase is considered as the continuum, and the solid phase is considered as the dispersed phase. The governing equations of gas and solid phase, heat transfer sub-models, and chemical reactions are detailed.

2.1. Governing equations for gas phase

The gas phase is solved through the volume-averaged governing equations. The mass, momentum, energy, and species conversation equations are calculated by [23]:

$$\frac{\partial(\varepsilon_g\rho_g)}{\partial t}+\nabla\cdot(\varepsilon_g\rho_g\mathbf{u}_g)=\sum_{n=1}^{N_g}R_{gn} \tag{1}$$

$$\frac{\partial(\varepsilon_g\rho_g\boldsymbol{u}_g)}{\partial t}+\nabla\cdot(\varepsilon_g\rho_g\boldsymbol{u}_g\boldsymbol{u}_g)=\nabla\cdot\bar{\bar{S}}_g+\rho_g\varepsilon_g\mathbf{g}-\sum_{m=1}^{M}\mathbf{I}_{gm} \tag{2}$$

$$\frac{\partial(\varepsilon_g\rho_g C_{p,g}T_g)}{\partial t}+\nabla\cdot(\varepsilon_g\rho_g\mathbf{u}_g C_{p,g}T_g)=\nabla\cdot(\varepsilon_g\kappa_g\nabla T_g)-Q_{gp}-\Delta H_{rg} \tag{3}$$

$$\frac{\partial(\varepsilon_g\rho_g X_n)}{\partial t}+\nabla\cdot(\varepsilon_g\rho_g\mathbf{u}_g X_n)=\nabla\cdot(\varepsilon_g\rho_g D_n\nabla X_n)+R_{gn} \tag{4}$$

where N_g is the total number of gas species. $\mathbf{u}_g$, ρ_g, and ε_g are the velocity, density, and volume fraction of the gas phase. R_{gn} and $= S_g$ are the volumetric generation rate of the n^{th} gas species and the gas stress tensor, respectively. $\mathbf{I}_{gm}$ is the interphase momentum exchange term between the m^{th} solid phase and the gas phase. T_g is the gas temperature. κ_g is the thermal conduction and $C_{p,g}$ is the specific heat of the gas phase. D_n and X_n are the diffusivity coefficient and mass fraction of the n^{th} gas species, respectively. ΔH_{rg} is the chemical reaction heat source and Q_{gp} is the convection heat transfer rate between gas and solid phases. Through the above quantities, the gas phase can be coupled with the solid phase, which are written as:

$$\begin{aligned}\varepsilon_g &= 1-\frac{1}{V_c}\sum_{i=1}^{N_p}V_{p,i}, \qquad \mathbf{I}_{gm}=\frac{1}{V_c}\sum_{i=1}^{N_p}\mathbf{f}_{d,i},\\ Q_{gp}&=\frac{1}{V_c}\sum_{i=1}^{N_p}Q_{gp,i}, \qquad R_{gn}=\frac{1}{V_c}\sum_{i=1}^{N_p}R_{gn,i}\end{aligned} \tag{5}$$

where V_c and $V_{p,i}$ are the volume of the current computational cell and the i^{th} particle, respectively. $R_{gn,i}$ is the mass consumption or generation rate of the i^{th} particle. $Q_{gp,i}$ is the convection heat transfer rate between the i^{th} particle and the gas phase.

2.2. Governing equations for solid phase

In the DEM method, particles can be tracked individually and their dynamics can be calculated using Newton's law of motion. The motion of i^{th} particle is calculated as [24]:

$$m_i\frac{d\mathbf{v}_i}{dt}=m_i\mathbf{g}+\mathbf{f}_{\nabla p}+\mathbf{f}_{d,i}+\mathbf{f}_{c,i} \tag{6}$$

$$I_i\frac{d\boldsymbol{\omega}_i}{dt}=\sum_{j=1,j\neq i}^{k}(L\mathbf{n}\times\mathbf{f}_{ct,ij}) \tag{7}$$

where $\boldsymbol{\omega}_i$ and $\mathbf{v}_i$ are the rotational and translational velocities, respectively. $\mathbf{f}_{\nabla p}$ is the pressure gradient force which relates to the fluid pressure gradient. L is the distance between the contact point and the particle center. $\mathbf{f}_{c,i}$ is the contact force acting on the i^{th} particle, which includes a normal component $\mathbf{f}_{n,ij}$ and a tangential component $\mathbf{f}_{t,ij}$ [25]:

$$\mathbf{f}_{c,i}=\sum_{j=1,j\neq i}^{N}(\mathbf{f}_{n,ij}+\mathbf{f}_{t,ij}) \tag{8}$$

$$\mathbf{f}_{n,ij}=-\left(k_{n,ij}\delta_{n,ij}+\eta_{n,ij}\dot{\delta}_{n,ij}\right)\mathbf{n}_{ij} \tag{9}$$

$$\mathbf{f}_{t,ij}=\begin{cases}-\left(k_{t,ij}\delta_{t,ij}-\eta_{t,ij}\dot{\delta}_{t,ij}\right)\mathbf{t}_{ij} \text{ for } |\mathbf{f}_{t,ij}|\leqslant\mu|\mathbf{f}_{n,ij}|\\ -\mu|\mathbf{f}_{n,ij}|\mathbf{t}_{ij} \text{ for } |\mathbf{f}_{t,ij}|>\mu|\mathbf{f}_{n,ij}|\end{cases} \tag{10}$$

where η, μ, and k are the damping coefficient, friction coefficient, and spring stiffness, respectively. The Linear spring-dashpot (LSD) model is chosen which has been proven to have higher efficiency compared with the non-linear Hertzian model [26]. The normal damping coefficient $\eta_{n,ij}$ can be calculated as [24]:

$$e_{n,ij}=\exp\left(-\frac{\eta_{n,ij}t_{n,ij}^{col}}{2m_{eff}}\right) \tag{11}$$

$$t_{n,ij}^{col}=\pi\left(\frac{k_{n,ij}}{m_{eff}}-\frac{\eta_{n,ij}^2}{m_{eff}^2}\right)^{-1/2} \tag{12}$$

$$\eta_{n,ij}=\sqrt{2k_{n,ij}m_{eff}}\,\frac{|\ln e_{n,ij}|}{\sqrt{\pi^2+\ln^2 e_{n,ij}}} \tag{13}$$

where $t_{n,ij}^{col}$ is the collision time. m_{eff} $(=m_im_j/(m_i+m_j))$ is the effective mass of i^{th} particle and j^{th} particle. $e_{n,ij}$ is the normal restitution coefficient. Similarly, the tangential damping coefficient $(\eta_{t,ij})$ can be calculated. $\mathbf{f}_{d,i}$ is drag force acting on i^{th} particle. In this work, the drag force is calculated based on the Gidaspow correlation, in which the fluid volume fraction is divided into two ranges [27]:

$$f_{d,i}=\frac{1}{V_c}\sum_{i=1}^{N_p}\left(\frac{\beta V_{p,i}}{1-\varepsilon_g}(\mathbf{u}_g-\mathbf{v}_i)\right) \tag{14}$$

$$\beta=\begin{cases}\dfrac{150(1-\varepsilon_g)^2\mu_g}{\varepsilon_g d_p^2}+1.75\dfrac{(1-\varepsilon_g)\rho_g|\mathbf{u}_g-\mathbf{v}_i|}{d_p}\varepsilon_g\leqslant 0.8\\ \dfrac{3}{4}\dfrac{\varepsilon_g(1-\varepsilon_g)\rho_g|\mathbf{u}_g-\mathbf{v}_i|}{d_p}C_D\varepsilon_g^{-2.65}\varepsilon_g>0.8\end{cases} \tag{15}$$

$$C_D=\begin{cases}\dfrac{24}{\mathrm{Re}_p}\left(1+0.15Re_p^{0.687}\right)Re_p<1000\\ 0.44Re_p\geqslant 1000\end{cases} \tag{16}$$

$$\mathrm{Re}_p=\frac{\rho_g\varepsilon_g|\mathbf{u}_g-\mathbf{v}_i|d_p}{\mu_g} \tag{17}$$

where C_D is the drag force coefficient related to the particle Reynolds number (Re_p). β is the momentum exchange coefficient.

2.3. Heat transfer sub-models

The heat transfer sub-models are coupled with the CFD-DEM

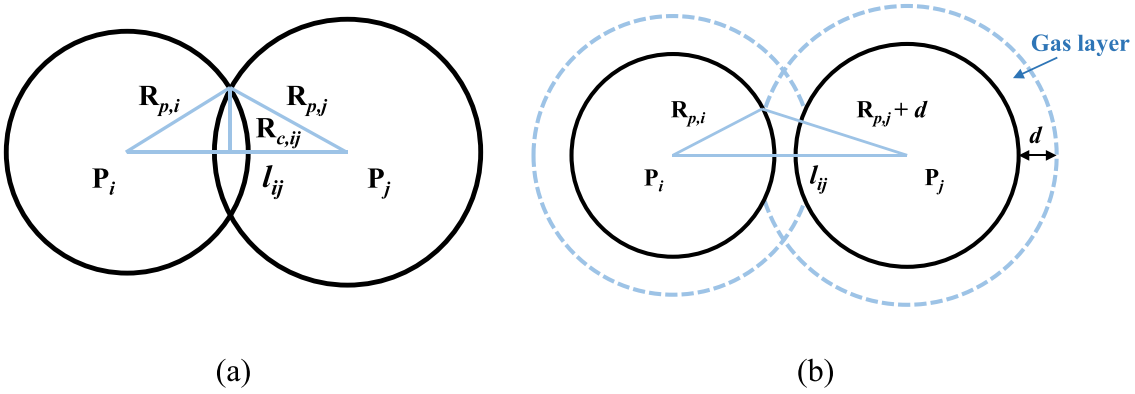

Fig. 2. Schematic diagram of particle–particle conduction (a) and particle–fluid-particle conduction.

framework. The particle is assumed to be isothermal without considering the temperature gradient inside the particle. The heat transfer of a particle can be classified into four modes: conduction, convection, radiation, and reaction. The energy conservation equation of particle is given as:

$$m_i C_{p,i}\frac{dT_{p,i}}{dt} = Q_{pp,i} + Q_{pgp,i} + Q_{gp,i} + Q_{rad,i} + \Delta H_{rs} \tag{18}$$

where ΔH_{rs} is the heat transfer rate caused by chemical reactions. Q represents the source term caused by different modes. The convective heat transfer rate $Q_{gp,i}$ is formulated as:

$$Q_{gp,i} = h_{pg,i}A_{p,i}\left(T_g - T_{p,i}\right) \tag{19}$$

$$h_{pg,i} = \frac{\mathrm{Nu}_{p,i}\kappa_g}{d_{p,i}} \tag{20}$$

$$\mathrm{Nu}_{p,i} = \begin{cases} 2 + 0.6\varepsilon_g^{3.5}\mathrm{Re}_{p,i}^{1/2}Pr^{1/3} & \mathrm{Re}_{p,i} < 200 \\ 2 + 0.5\varepsilon_g^{3.5}\mathrm{Re}_{p,i}^{1/2}Pr^{1/3} + 0.02\varepsilon_g^{3.5}\mathrm{Re}_{p,i}^{0.8}Pr^{1/3} & 200 < \mathrm{Re}_{p,i} < 1500 \\ 2 + 0.000045\varepsilon_g^{3.5}\mathrm{Re}_{p,i}^{1.8} & \mathrm{Re}_{p,i} > 1500 \end{cases} \tag{21}$$

where $A_{p,i}$ stands for particle surface area. $h_{pg,i}$ is the convection heat transfer coefficient. Particle Nusselt number ($\mathrm{Nu}_{p,i}$) is related to Prandtl number Pr ($=\mu_g C_{p,g}/\kappa_g$) and $\mathrm{Re}_{p,i}$ [28].

As shown in Fig. 2, the conductive heat transfer can be classified as two paths, i.e., particle–particle conduction ($Q_{pp,i}$) and particle–fluid-particle conduction ($Q_{pfp,i}$). As a direct heat transfer path, the former one occurs when two particles collide and is formulated as [29]:

$$Q_{pp,ij} = 4\frac{\kappa_{p,i}\kappa_{p,j}}{\kappa_{p,i} + \kappa_{p,j}}R_{c,ij}\left(T_{p,j} - T_{p,i}\right) \tag{22}$$

$$R_{c,ij} = \sqrt{R_{p,j}^2 - \left(\frac{R_{p,j}^2 - R_{p,i}^2 + l_{ij}^2}{2l_{ij}}\right)^2} \tag{23}$$

where $R_{c,ij}$ is the radius of the particle contact surface. $\kappa_{p,i}$ and $\kappa_{p,j}$ denote the thermal conductivity for the i^{th} particle and j^{th} particle, respectively.

Similarly, if two particles are very close, $Q_{pfp,i}$ are considered to transfer through a gas layer wrapping the particle, as shown in Fig. 2(b). The thickness of the gas layer is assumed to be 0.2 $R_{p,i}$, and $Q_{pfp,i}$ can be calculated as [30]:

$$Q_{pgp,ij} = \kappa_g\left(T_{p,j} - T_{p,i}\right)\int_{R_{in}}^{R_{out}} \frac{2\pi r}{l_{ij} - \left(\sqrt{R_{p,i}^2 - r^2} + \sqrt{R_{p,j}^2 - r^2}\right)}dr \tag{24}$$

$$R_{in} = R_{c,ij} = \begin{cases} 0 l_{ij} > \left(R_{p,i} + R_{p,j}\right) \\ \sqrt{R_{p,j}^2 - \left(\frac{R_{p,j}^2 - R_{p,i}^2 + l_{ij}^2}{2l_{ij}}\right)^2} \; l_{ij} \leqslant \left(R_{p,i} + R_{p,j}\right) \end{cases} \tag{25}$$

$$R_{out} = R_{f,ij} = \sqrt{\left(R_{p,j} + d\right)^2 - \left(\frac{\left(R_{p,j} + d\right)^2 - R_{p,i}^2 + l_{ij}^2}{2l_{ij}}\right)^2} \tag{26}$$

where R_{in} and R_{out} are the integral bounds of the contact region, respectively.

If the reacting system operates under high temperature (>600 ℃), the radiation heat transfer should be considered which occurs between particle and surrounding particles in a sub-domain. Thus, the environmental temperature (T_{env}) can be obtained based on gas temperature and mean particle temperature in the sub-domain [31]. $Q_{rad,i}$ is calculated related to T_{env} and given as:

$$Q_{rad,i} = e_{p,i}A_{p,i}\sigma\left(T_{env}^4 - T_{p,i}^4\right) \tag{27}$$

$$T_{env} = \varepsilon_g T_{g,\Omega} + \left(1 - \varepsilon_g\right)\frac{1}{N_{p,\Omega}}\sum_{j=1,j\neq i}^{N_{p,\Omega}} T_j \tag{28}$$

where $e_{p,i}$ is effective emissivity. $N_{p,\Omega}$ and $T_{g,\Omega}$ are the number of particles and the gas temperature in the sub-domain, respectively. σ is the Stefan-Boltzmann constant.

As for the heat transfer caused by chemical reactions, the heat is composed of that related to the solid phase (ΔH_{rs}) and the gas phase (ΔH_{rg}). For both ΔH_{rg} and ΔH_{rs}, the heat is obtained because of the difference in enthalpies of the gaseous or solid reactants and products. They are generally formulated as:

$$\Delta H_r = \sum H_{n,products} - \sum H_{n,reactants} \tag{29}$$

Furthermore, the enthalpy change of n^{th} species at temperature T can be obtained by:

$$H_n(T) = H_n^o\left(T_{ref}\right) + \int_{T_{ref}}^{T} C_{pn}dT \tag{30}$$

where C_{pn} is the specific heat capacity. $H_n^o\left(T_{ref}\right)$ is the enthalpy for n^{th} species at reference temperature T_{ref}.

2.4. Chemical reactions

Based on the state of reactants and products, the chemical reactions that take place in fluidized beds can be classified as heterogeneous reactions and homogenous reactions. The former is calculated at the

Table 1
Chemical reactions and reaction rates [39–42].

Gasification reaction	Reaction rates	
R1 Char + CO_2 → 2CO + 0·.0365H_2 + 0·.026H_2O	$r_{CO_2} = \frac{k_{CO_2}K_{CO_2}P_{CO_2}}{1+K_{CO_2}P_{CO_2}+K_{CO}P_{CO}}$	$\dot{m}_{Char} = \rho_p\varepsilon_p\frac{A_p}{1-\varepsilon_0}r_n(1-X_p)^{2/3}$
R2 Char + H_2O → 1.073H_2 + CO + 0·.026H_2O	$r_{H_2O} = \frac{k_{H_2O}K_{H_2O}P_{H_2O}}{1+K_{H_2O}P_{H_2O}+K_{H_2}P_{H_2}}$	
Water-gas-shift reaction		
R3 CO + H_2O → H_2 + CO_2	$r_{WGS} = -k_0\left(e^{-E/RT}C_{H_2}^{0.5}C_{CO_2} - \frac{1}{\exp(-4.33+4577.8/T)}e^{-E/RT}C_{H_2O}C_{CO}\right)$	
Metal oxide reduction reaction		
R4 $3Fe_2O_3$ + CO → $2Fe_3O_4$ + CO_2	$\dot{m}_{CO} = \frac{k_{CO}R_0}{2M_{O_2}}\rho_p\varepsilon_p\left(X_{Fe_2O_3}+X_{Fe_3O_4}\times\frac{3M_{Fe_2O_3}}{2M_{Fe_3O_4}}\right)(1-\xi)^{2/3}M_{CO}$	
R5 $3Fe_2O_3$ + H_2 → $2Fe_3O_4$ + H_2O	$\dot{m}_{H_2} = \frac{k_{H_2}R_0}{2M_{O_2}}\rho_p\varepsilon_p\left(X_{Fe_2O_3}+X_{Fe_3O_4}\times\frac{3M_{Fe_2O_3}}{2M_{Fe_3O_4}}\right)(1-\xi)^{2/3}M_{H_2}$	

particle scale and the latter is solved at the grid scale. The particle mass conservation equation can be evaluated as:

$$\frac{dm_i}{dt} = \sum_{n=1}^{N_p} R_{sn} \tag{31}$$

where N_p is the total number of solid species in the i^{th} particle. R_{sn} is the production or consumption rate of species n in the i^{th} particle. The progressive conversion model and shrinking core model are two representations of particle conversion models [7]. The former is suitable for highly porous particles due to the assumption that the gas phase reactants diffuse evenly into the particle before reacting with the pore surface. Thus, the solid phase reactant reduces evenly as the reaction proceeds. Comparable, in the latter, the density of the particle is considered as a fixed value and the particle diameter decreases because of the solid products "flaking-off" from the surface of the particle. Thus, the shrinking core model is adopted to calculate the diameter of the particle, which has been widely used in simulating chemical reaction processes in fluidized beds [32–35]. The particle diameter during the chemical reactions can be given as:

$$d_p = \left(\frac{6m_i}{\pi\rho_p}\right)^{1/3} \tag{32}$$

When the particle centroid method (PCM) is used in the CFD-DEM method, the grid size (Δx) should be 3 ~ 5 times the particle diameter (d_p) to avoid inaccuracy at cell boundaries with fine grids [36,37]. Thus, when the grid size remains unchanged, CFD-DEM can also maintain the

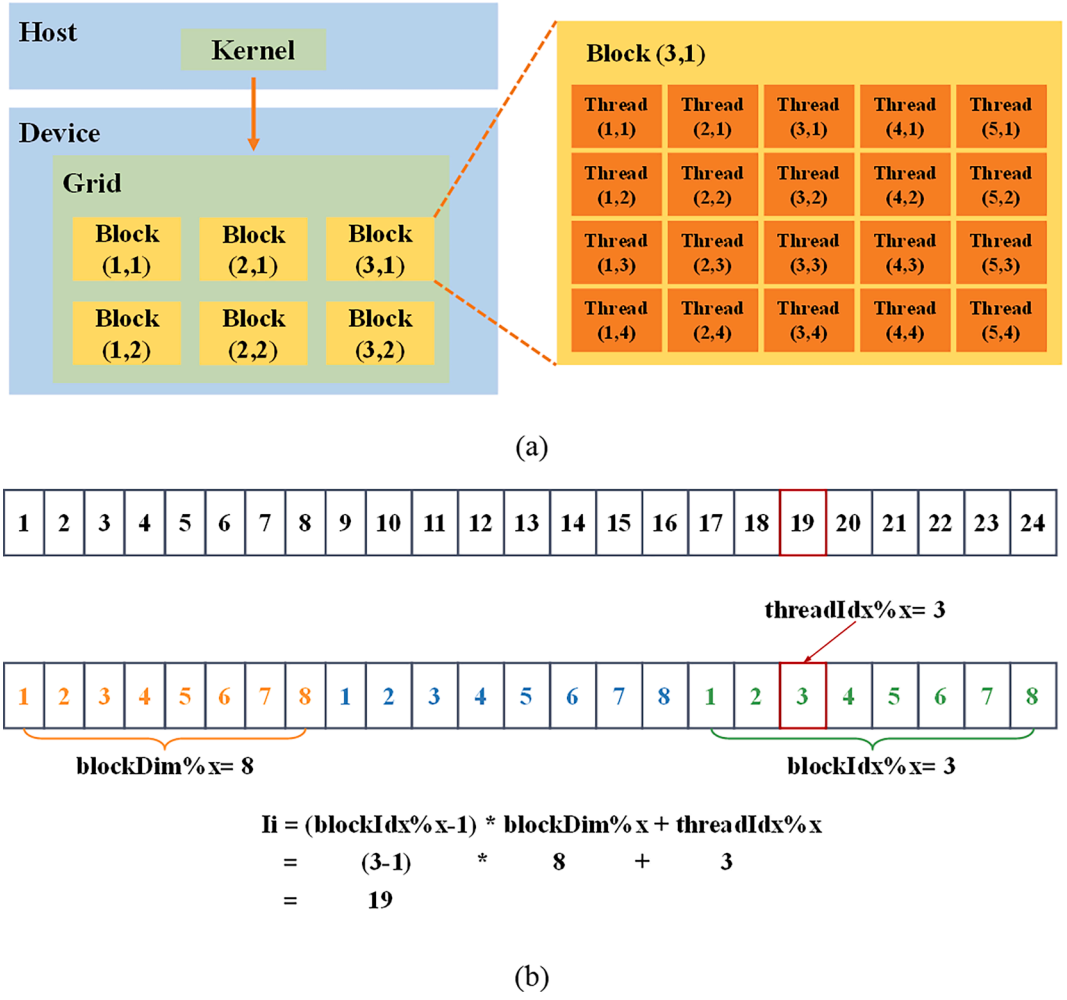

Fig. 3. Schematic diagram of the typical call structure of the GPU-accelerated CFD-DEM reactive model (a) and the representation of thread ID (b).

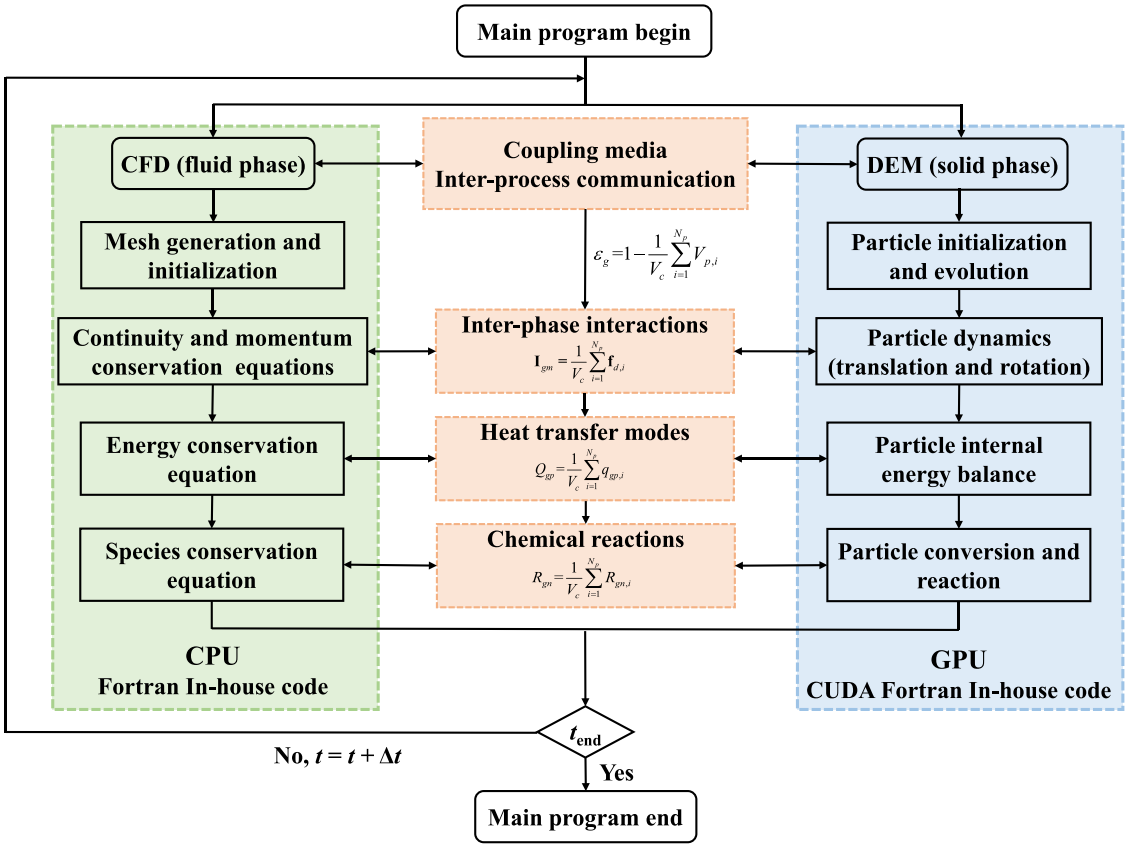

Fig. 4. Schematic diagram of the coupling procedure of the GPU-accelerated CFD-DEM reactive model.

same accuracy even with smaller particle diameters. To avoid the huge amounts of computational time on particle collision detection for large particles when the particle's diameter becomes too small, the particle is removed from the calculation when its diameter decreases to a threshold value of its original diameter. Therefore, the grid size and particle diameter are always within reasonable ranges.

Taking coal-fueled chemical-looping gasification (CLG) for example, the solid fuel is coal char and oxygen carriers are composed of Fe_2O_3 and Al_2O_3. The reactions considered include the char gasification reactions (R1, R2), the water–gas-shift reaction (R3), and the metal oxide reduction reactions (R4, R5). The chemical reactions and reaction rates are detailed in Table 1. More detailed kinetic parameters can be found in our previous work [38].

2.5. GPU implementation

Although the CFD-DEM method has been paralleled on Central Processing Unit (CPU) multi-cores, it still has limitations in simulating large-scale chemical reaction systems due to the high-frequency particle collision and complex thermochemical behavior. Compared to CPU, GPU can provide much higher instruction throughout and memory bandwidth [43]. Furthermore, GPU is designed with plenty of stream multiprocessor (SM) composed of GPU cores for highly parallel computations. The introduction of CUDA makes it possible to solve complex computing problems in a more efficient way than the CPU. To achieve better performance, the CPU and GPU can be coupled to complete the complex calculation, which is called heterogeneous computing. Algorithm 1 presents the sample code of the GPU-accelerated particle–fluid convection heat transfer method. The code consists of the host code on the CPU and the device code on the GPU. The latter is defined as a kernel through the *attributes(global)* declaration specifier. Each thread is given a unique thread ID based on the execution configuration and used to calculate a particle in the system. The number of GPU threads used in the calculation should be the same as the number of particles in the system (N) and is specified using a $<<<gridsize,\ blocksize>>>$ execution configuration syntax. Fig. 3(a) presents the typical call structure of the GPU-accelerated CFD-DEM method. One kernel can correspond to only one grid while one grid can be constructed by many blocks and one block can be constructed by many threads. As a three-dimensional (3D) vector, threadIdx can be identified using a one/two/three-dimensional thread index and forming a one/two/three-dimensional thread block based on the computational need. Referring to Fig. 3(b), the thread ID for a one-dimensional (1D) block and thread can be calculated based on the length of a block (blockDim%x), the index of thread in the block (threadIdx%x), and the index of the block (blockIdx%x).

Algorithm 1. Sample code of GPU-accelerated particle–fluid convection heat transfer method.

```
N: The number of particles.
// Kernel definition
module heat-transfer
contains
  attributes(global) subroutine convection(N)
    implicit none
    integer:: Ii
    integer:: N
    Ii = threadIdx%x + (blockIdx%x-1) * blockDim%x
    if (Ii ≤ N) then
        Q_gp,i = h_pg,i A_p,i (T_g − T_p,i)
    endif
  end subroutine convection
end module heat-transfer
program main
  use heat-transfer
  use cudafor
  implicit none
  type(dim3):: gridsize, blocksize
  gridsize = dim3(N/x + 1,1,1)
```

(*continued on next page*)

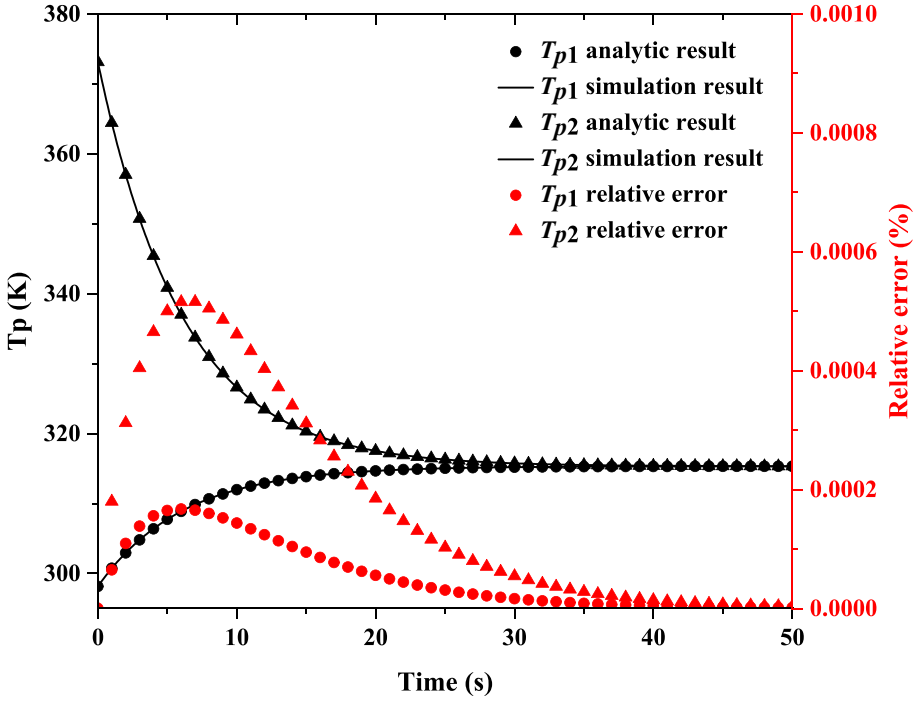

Fig. 5. Numerical comparison of analytic results and simulation results for particle–particle conduction.

(*continued*)

```
    blocksize = dim3(x,y,z)
    // Kernel invocation
    call convection<<<gridsize, blocksize>>>(N)
end program main
```

2.6. Numerical scheme

Fig. 4 presents the coupling procedure of the GPU-accelerated CFD-DEM reactive model. The fluid phase is solved on the CPU and the particle phase is parallelly calculated on GPU. The data on gas properties and particle properties are stored in CPU memory and GPU memory, respectively. Through information communication, the CFD module and DEM module can be coupled to numerically study dense gas–solid reacting flow. To minimize the unavoidable time consumption during the data transfer process, the pinned memory is adopted which can significantly reduce the time of data transfer between CPU and GPU. The particle information is mapped into the calculation grid to calculate the inter-phase interaction force, initial void fraction, heat transfer rates, and species consumption before each time-step. Then the CFD solver does iteration to solve gas phase. The coupling between the velocity and pressure of the gas phase is solved using the SIMPLE algorithm, which is a widely used implicit pressure-based scheme for Navier-Stokes equations. Since proposed by Patankar and Spalding [44], the SIMPLE algorithm not only provided a remarkably successful implicit method but has dominated for decades the field of numerical simulation of incompressible flows. Efficient and iterative solvers based on the SIMPLE Algorithm have been developed within the framework of the finite-volume method, demonstrating reliable and widely applicable results [17,45,46]. The governing equations for species and temperature are solved by checking numerical convergence. When the convergence is achieved after several iterations, it's time to calculate chemical reactions. Thus, the gas information of each computational grid can be obtained. For the DEM solver, the drag force is firstly obtained referred to the gas information transfer from CPU to GPU. Then the diameter, and mass are obtained by solving the chemical reaction rates. The position and velocity of the particle are calculated by solving the particle motion equation. The temperature of the particle is obtained by solving the particle energy equation.

The finite volume method (FVM) is adopted to discretize the governing equations of the gas phase, which are integrated through the first-order Euler scheme. During the calculation process, the gas time-step (Δt_{CFD}) is established referred to the Courant-Friedrich-Lewy (CFL) condition, which is given by [47]:

$$\mathrm{CFL} = \Delta t_{CFD} \max\left(\frac{|\mathbf{u}_f|}{\Delta x}\right) < 1 \tag{33}$$

where Δx is the characteristic size of grid. The minimum and maximum Δt_{CFD} should be preestablished to guarantee efficiency and convergence. The Δt_{CFD} should be an order of magnitude larger than the solid time-step (Δt_{DEM}) to guarantee numerical stability. In this work, the Δt_{DEM} is specified as 1/50 of the minimum collision time ($t_{n,ij}^{col}$) [48]. Thus, the DEM solver makes loops that advance the solid simulation time to the gas simulation time. The CFD solver and DEM solver are coupled at each Δt_{CFD} through the source terms of voidage, force interactions, heat transfer, and chemical reactions. Note that the heat transfer and chemical reactions take place instantly.

3. Model verification

It is of great importance to guarantee the simulation accuracy of the developed model. Thus, in this section, a series of verification studies are given to verify the accuracy of thermochemical sub-models. Specifically, the simulation results of individual particle are compared with the analytic solutions. Moreover, to avoid the mutual influence, when one heat transfer sub-model is being verified, the other heat transfer sub-models are not considered.

3.1. Particle-particle conduction

The particle–particle conduction is firstly verified because of the severe particle–particle collisions in dense gas–solid systems. Two particles are set at different temperatures and the temperature are 373.15 K (T_{p1}) and 278.15 K (T_{p2}), respectively. The positions of two particles are assumed to be fixed. Detailed particle properties are given in Table S2 of

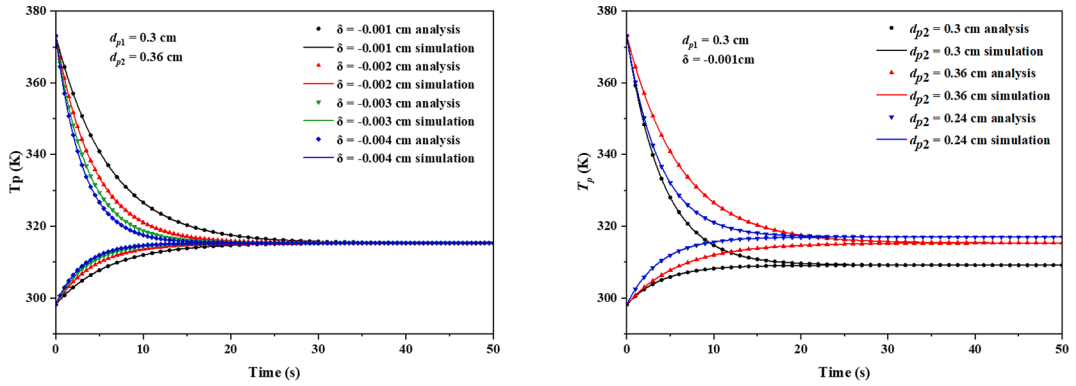

(a) (b)

Fig. 6. Numerical comparison of analytic results and simulation results: change particle overlap displacement (a) and change particle diameter (b).

the Supporting Information. Each simulation runs for 50 s thus the particles can reach a steady temperature.

In this case, only particle–particle conduction is considered. Thus, the temperature of each particle can be calculated by simplifying Eq. (18):

$$\frac{dT_{p,i}}{dt} = \frac{4\kappa_{p,i}\kappa_{p,j}}{\kappa_{p,i}+\kappa_{p,j}} \frac{T_{p,i}-T_{p,j}}{m_i C_{p,i}} \sqrt{R_{p,j}^2 - \left(\frac{R_{p,j}^2 - R_{p,i}^2 + l_{ij}^2}{2l_{ij}}\right)^2} \tag{34}$$

As the benchmark for comparison, the analytic temperature can be calculated as [30]:

$$T_{p,i}(t) = \frac{1}{a+b}\left[bT_{p,i}^0 + aT_{p,j}^0 + a\left(T_{p,i}^0 - T_{p,j}^0\right)e^{-(a+b)t}\right] \tag{35}$$

$$T_{p,j}(t) = \frac{1}{a+b}\left[bT_{p,i}^0 + aT_{p,j}^0 - b\left(T_{p,i}^0 - T_{p,j}^0\right)e^{-(a+b)t}\right] \tag{36}$$

where a and b are the computational constants related to the characteristics of particles and are formulated as:

$$a = \frac{2}{m_i C_{p,i}} \frac{\kappa_{p,i}\kappa_{p,j}}{\kappa_{p,i}+\kappa_{p,j}} \sqrt{R_{p,j}^2 - \left(\frac{R_{p,j}^2 - R_{p,i}^2 + l_{ij}^2}{2l_{ij}}\right)^2} \tag{37}$$

$$b = \frac{2}{m_j C_{p,j}} \frac{\kappa_{p,i}\kappa_{p,j}}{\kappa_{p,i}+\kappa_{p,j}} \sqrt{R_{p,j}^2 - \left(\frac{R_{p,j}^2 - R_{p,i}^2 + l_{ij}^2}{2l_{ij}}\right)^2} \tag{38}$$

Fig. 5 presents the numerical comparison of analytic results and simulation results for particle–particle conduction. The thermal energy transfers through the overlap area until at the same temperatures. After about 30 s, the particle temperatures reach a fixed value. The simulation results are in line with analytic results. The relative error between analytic results and simulation results ($e = \left|\frac{T_p^a - T_p^s}{T_p^a}\right| \times 100\%$) is smaller than 0.0006 %, which indicates the accuracy of the current model in predicting particle–particle conduction heat transfer.

To better illustrate the effect of the overlap displacement, the overlap displacement is set as different values (i.e., 0.001/0.002/0.003/0.004 cm). Furthermore, to verify the universality of the current model, two particles in the same or different particles (i.e., $d_{p1} = 0.3$ cm, $d_{p2} = 0.24$/0.3/0.36 cm) are also considered. Fig. 6 presents the comparison of analytic results and simulation results under different simulation conditions. Simulation results agree well with analytic results under all simulation conditions. Specifically, with the increase of the overlap displacement, the particle–particle conduction heat transfer is more intense and the particles reach the final temperature faster. However,

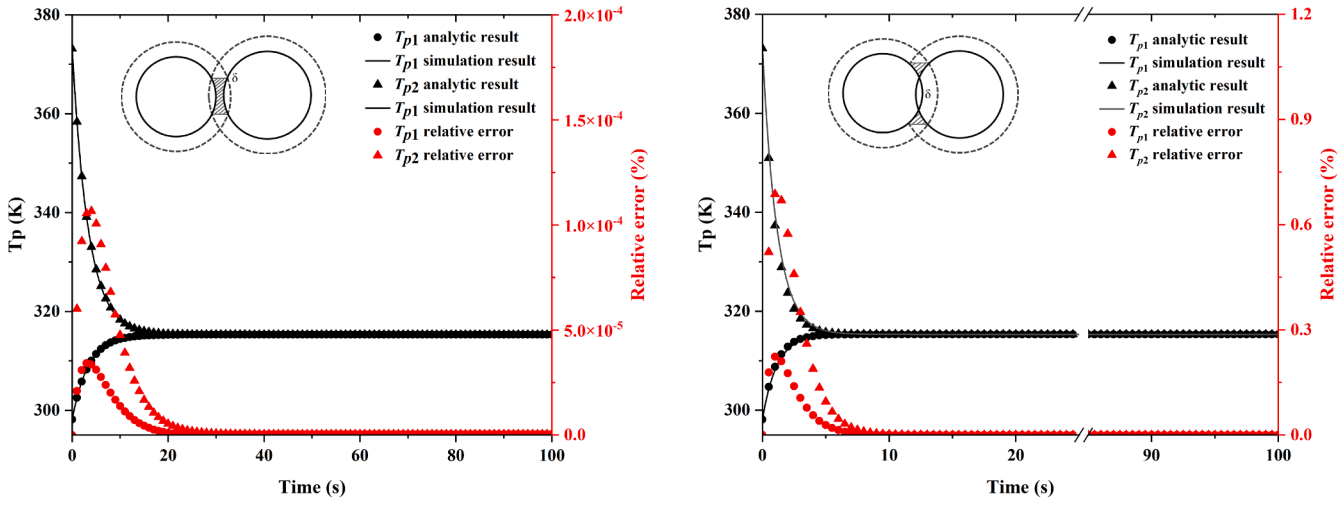

(a) (b)

Fig. 7. Numerical comparison of analytic results and simulation results for particle–fluid-particle conduction: untouched particle (a) and touched particle (b).

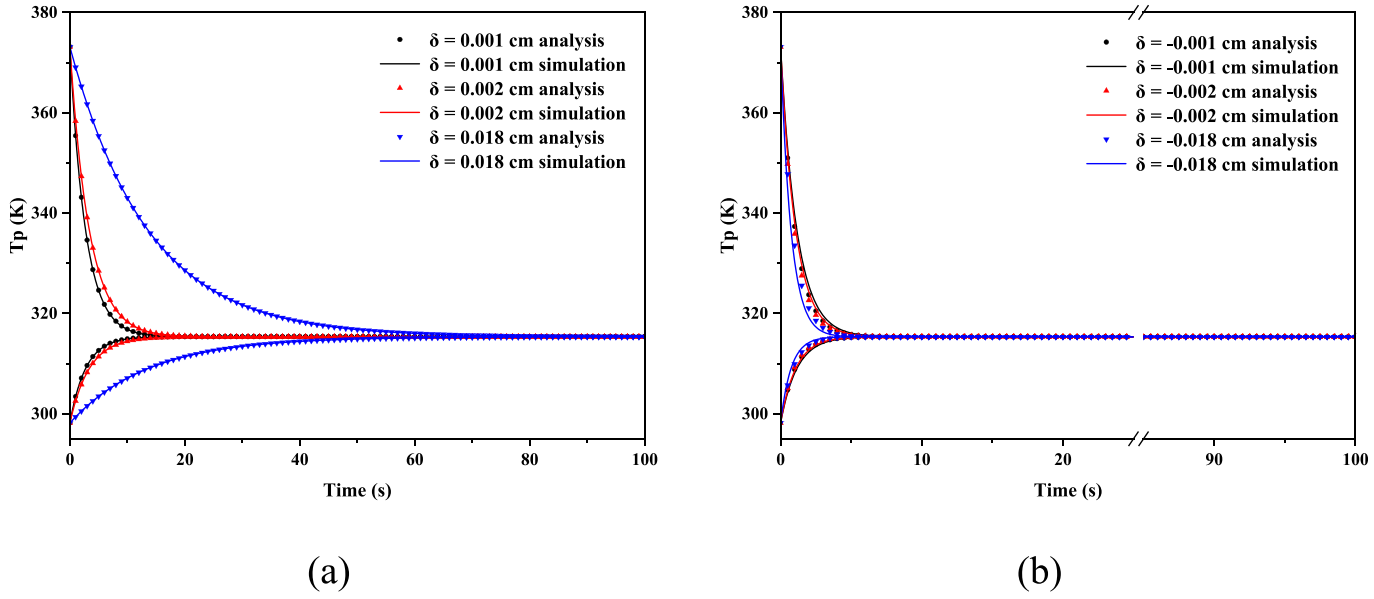

Fig. 8. Numerical comparison of analytic results and simulation results for particle–fluid-particle conduction: untouched particle (a) and touched particle (b).

changing overlap displacement has an insignificant influence on the final particle temperature. While changing particle diameter, the final temperature of two particles is different. When the particles are in different diameters, the final temperature is higher than that under the same diameters. Thus, the current model can accurately simulate the particle–particle conduction.

3.2. *Particle-fluid-particle conduction*

The thermal energy can also transfer through particle–fluid-particle conduction in dense particle systems. Specifically, it contains two subcases: two particles not in contact but in close proximity and two particles in contact (referred to Fig. 7). The simulation setup and characteristics of the particles are the same as the previous section. The thickness of the gas layer wrapping the particle is 0.036 cm (0.1 d_{p2}). Each simulation runs for 100 s to guarantee a steady state of particle temperature.

Eq. (18) can be simplified when only considering the particle–fluid-particle conduction heat transfer and the temperature of each particle can be calculated as:

$$\frac{dT_{p,i}}{dt}=\frac{\kappa_g\left(T_{p,j}-T_{p,i}\right)}{m_i C_{p,i}}\int_{R_{in}}^{R_{out}}\frac{2\pi r}{l_{ij}-\left(\sqrt{R_{p,i}^2-r^2}+\sqrt{R_{p,j}^2-r^2}\right)}dr \tag{39}$$

As the benchmark for comparison, the analytic temperature can be calculated as [30]:

$$T_{p,i}(t)=\frac{1}{a+b}\left[bT_{p,i}^0+aT_{p,j}^0+a\left(T_{p,i}^0-T_{p,j}^0\right)e^{-(a+b)t}\right] \tag{40}$$

$$T_{p,j}(t)=\frac{1}{a+b}\left[bT_{p,i}^0+aT_{p,j}^0-b\left(T_{p,i}^0-T_{p,j}^0\right)e^{-(a+b)t}\right] \tag{41}$$

where a and b are the computational constants and are formulated as:

$$a=\frac{\kappa_g}{m_i C_{p,i}}\int_{R_{in}}^{R_{out}}\frac{2\pi r}{l_{ij}-\left(\sqrt{R_{p,i}^2-r^2}+\sqrt{R_{p,j}^2-r^2}\right)}dr \tag{42}$$

$$b=\frac{\kappa_g}{m_j C_{p,j}}\int_{R_{in}}^{R_{out}}\frac{2\pi r}{l_{ij}-\left(\sqrt{R_{p,i}^2-r^2}+\sqrt{R_{p,j}^2-r^2}\right)}dr \tag{43}$$

Fig. 7 presents the comparison of analytic results and simulation results. For the untouched particle, the thermal flux transfers through the shadow region, as shown in Fig. 8(a). After about 20 s, the temperature of two particles reaches a steady value. The simulation results agree well with analytic results and the relative error is less than 0.00015 %. However, as for the touched particles, a significant relative error can be observed. The reason may lie in that the thermal flux is passed through the shadow region in Fig. 8(b). The computational constant a and b of analytic results is calculated by solving the integral referring to Eqs. (41) and (42). The error caused by the integral solution leads to a decrease of the accuracy of analytic results. Thus, the current model can accurately simulate the particle–fluid-particle conduction.

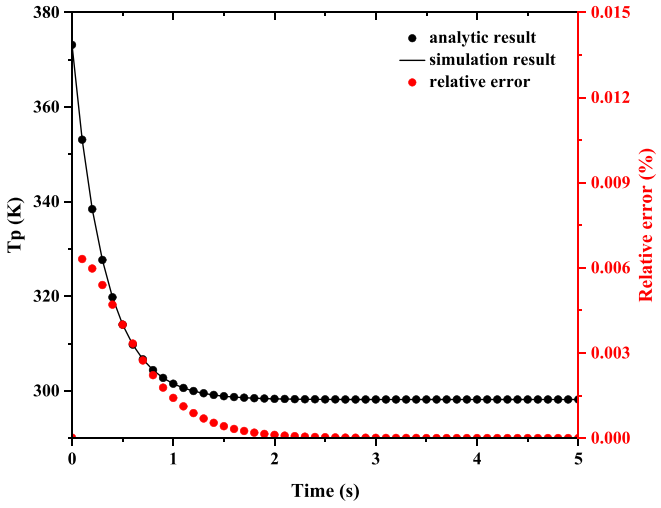

Fig. 9. Numerical comparison of analytic results and simulation results for particle–fluid convection.

The overlap displacement is set as different values (i.e., 0.001 cm, 0.002 cm, and 0.018 cm) to further discuss the influences of inter-particle distance and overlap displacement. As shown in Fig. 8, changing the overlap displacement significantly influence the temperature evolution for the untouched particles. With the increase of displacement, the heat transferred through the shadow region decreases. When the maximum displacement is 0.018 cm (0.1 d_{p2}), particle temperature evaluates to the fixed value at about 70 s. However, changing

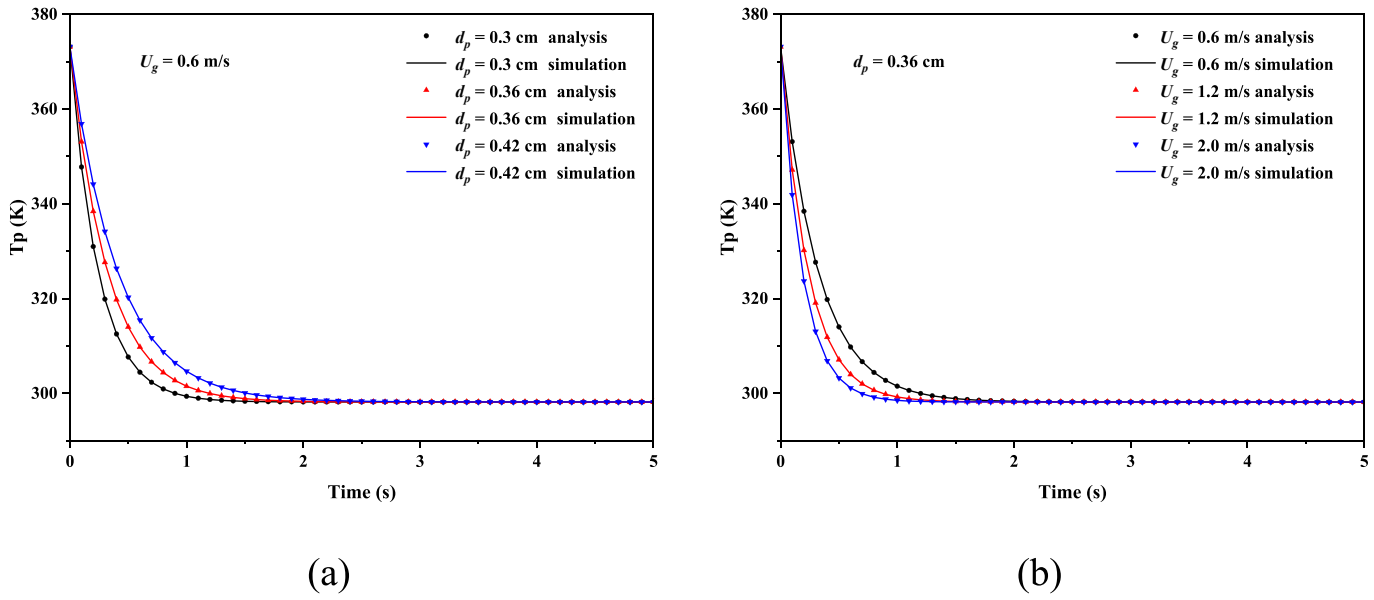

Fig. 10. Numerical comparison of analytic results and simulation results for particle–fluid convection: change particle diameter (a) and change fluid velocity (b).

displacement has a negligible influence on touched particles due to the slight change.

3.3. Particle-fluid convection

Fig. 9 presents the comparison of analytic results and simulation results for particle–fluid convection. The diameter of the particle is 0.36 cm and the particle position is fixed. The fluid was introduced from the bottom of the system and the velocity is 0.6 m/s. The temperature of the particle and fluid are 373.15 K and 298.15 K, respectively. The simulation results and analytic results of the particle temperature are respectively formulated as:

$$\frac{dT_{p,i}}{dt} = \frac{h_{pg,i}A_{p,i}\left(T_g - T_{p,i}\right)}{m_i C_{p,i}} \tag{44}$$

$$T_{p,i}(t) = T_g - \left(T_g - T_{p,i}^0\right) e^{-\frac{h_{pg,i}A_{p,i}}{m_i C_{p,i}} t} \tag{45}$$

As shown in Fig. 9, simulation results agree well with analytic results, indicating the accuracy of the current model in simulating the particle–fluid convection. The particle temperature decreases to the fluid temperature at about 1 s. Referring to Eq. (41), the convective heat transfer is calculated based on the particle surface area and convective heat transfer coefficient. Thus, the influences of particle diameter and fluid velocity on convective heat transfer are numerically studied. As

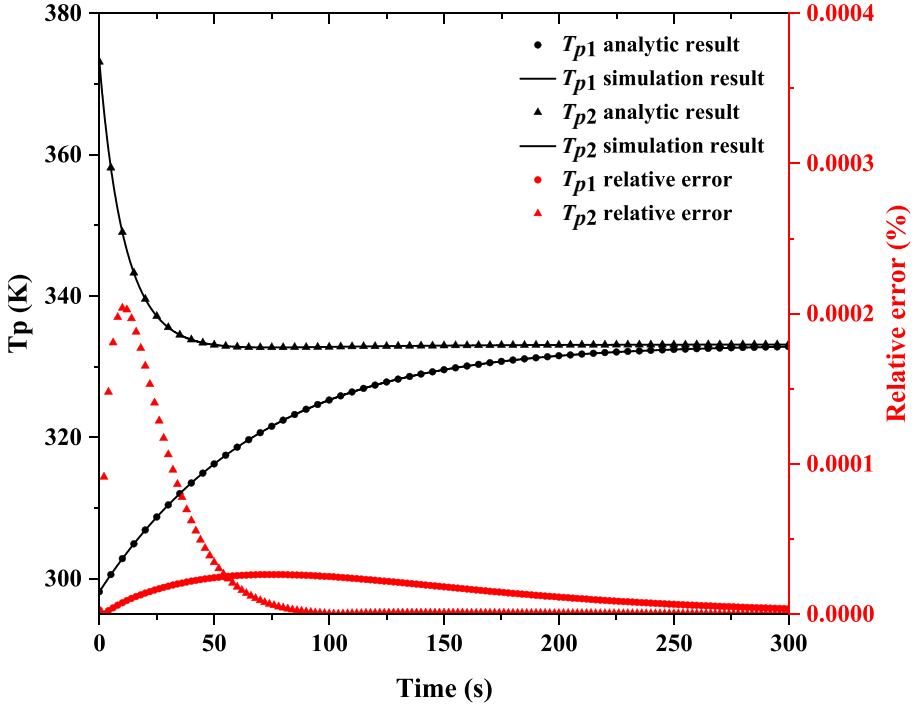

Fig. 11. Numerical comparison of analytic results and simulation results for radiation.

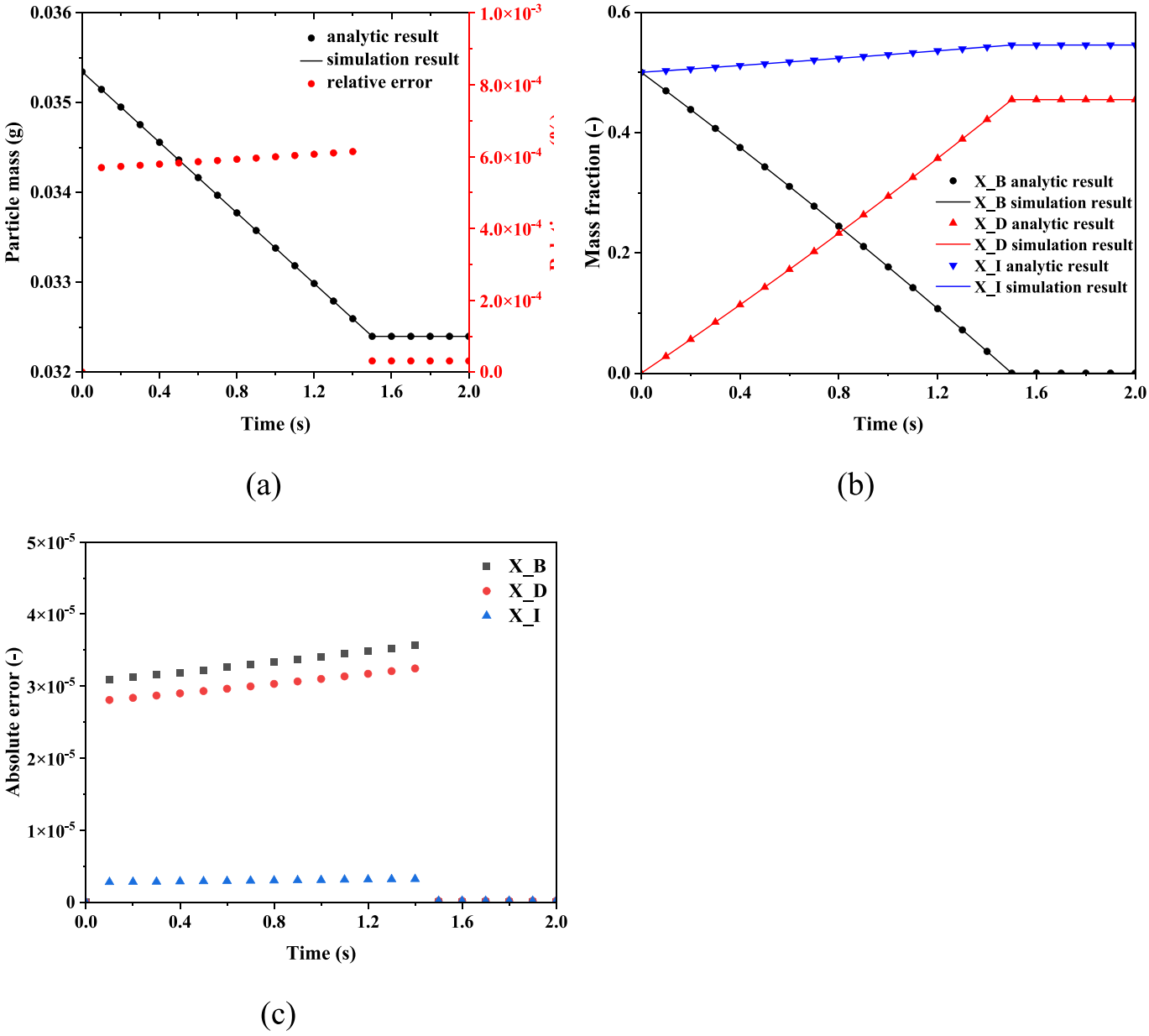

Fig. 12. Numerical comparison of analytic results and simulation results for the chemical reaction: the particle mass (a), species mass fraction (b), and absolute error of species mass fraction (c).

shown in Fig. 10, the temperature of smaller particle decreases to the environmental temperature faster. Moreover, increasing the fluid velocity can intensify the particle–fluid convection due to the increase of relative velocity ($\mathbf{u}_g$ - $\mathbf{v}_i$).

3.4. Particle radiation

The radiation heat transfer is verified through two particles at different temperatures. Specifically, the two particles are fixed and close to each other. The particle properties are the same as the case of particle–particle conduction. The simulation runs for 300 s and the particle temperature can reach a steady value. In the simulation, only radiation heat transfer is considered, thus Eq. (18) can be simplified and the particle temperature can be calculated as:

$$\frac{dT_{p,i}}{dt} = \frac{e_{p,i}A_{p,i}\sigma\left(T_{env}^4 - T_{p,i}^4\right)}{m_i C_{p,i}} = f\left(t, T_{p,i}, T_{p,j}\right) \tag{46}$$

However, the analytic results of particle temperature are difficult to obtain due to the nonlinear dependence. Thus, the standard fourth-order Runge-Kutta method is adopted to calculate the particle temperature for comparison, which is formulated as [30]:

$$\begin{cases} T_{p,i}(t_{n+1}) = T_{p,i}(t_n) + \dfrac{1}{6}\left(k_{1,i} + 2k_{2,i} + 2k_{3,i} + k_{4,i}\right) & where\ T_{p,i}(t_0) = T_{p,i}^0 \\ T_{p,j}(t_{n+1}) = T_{p,j}(t_n) + \dfrac{1}{6}\left(k_{1,j} + 2k_{2,j} + 2k_{3,j} + k_{4,j}\right) & where\ T_{p,j}(t_0) = T_{p,j}^0 \end{cases} \tag{47}$$

$$\begin{cases} k_1 = \Delta t f\left(t_n, T_{p,i}(t_n), T_{p,j}(t_n)\right) \\ k_2 = \Delta t f\left(t_n + \dfrac{\Delta t}{2}, T_{p,i}(t_n) + \dfrac{k_{1,i}}{2}, T_{p,j}(t_n) + \dfrac{k_{1,j}}{2}\right) \\ k_3 = \Delta t f\left(t_n + \dfrac{\Delta t}{2}, T_{p,i}(t_n) + \dfrac{k_{2,i}}{2}, T_{p,j}(t_n) + \dfrac{k_{2,j}}{2}\right) \\ k_4 = \Delta t f\left(t_n + \Delta t, T_{p,i}(t_n) + k_{3,i}, T_{p,j}(t_n) + k_{3,j}\right) \end{cases} \tag{48}$$

Fig. 11 illustrates the comparison of analytic results and simulation results. After about 250 s, the temperatures of two particles reach steady values. The relative error is less than 0.00002 %, indicating the accuracy of the current model in predicting particle radiation.

3.5. Chemical reaction

Besides the heat transfer sub-models, the verification of chemical reactions is also of great importance. In this section, a specified heterogeneous reaction is given by:

$$\mathrm{A(g)} + 2\mathrm{B(s)} \rightarrow \mathrm{C(g)} + \mathrm{D(s)} \tag{49}$$

where A and C are the gaseous substances while B and D are active solid substances. At the initial time, the particle contains B and the inert solid phase I. The reaction rate is assumed as the disappearance rate of B ($-r_\mathrm{B}$) and is set as constant. The reaction or formation rate of each species is given by:

$$\frac{-r_\mathrm{A}}{\mathrm{M_A}} = \frac{1}{2}\frac{-r_\mathrm{B}}{\mathrm{M_B}} = \frac{r_\mathrm{C}}{\mathrm{M_C}} = \frac{r_\mathrm{D}}{\mathrm{M_D}} \tag{50}$$

where r_i and M_i represent the reaction rate and mass of each species i, respectively. The particle mass and species mass fraction (X_i) can be calculated as:

$$\frac{dm_p}{dt} = -r_\mathrm{B}\left(\frac{1}{2}\frac{\mathrm{M_D}}{\mathrm{M_B}} - 1\right) \tag{51}$$

$$\begin{aligned} &\frac{d}{dt}\left(X_\mathrm{B} m_p\right) = -(-r_\mathrm{B}), \\ &\frac{d}{dt}\left(X_\mathrm{D} m_p\right) = \frac{1}{2}\frac{\mathrm{M_D}}{\mathrm{M_B}}(-r_\mathrm{B}), \quad \frac{d}{dt}\left(X_\mathrm{I} m_p\right) = 0 \end{aligned} \tag{52}$$

As the benchmark for comparison, the analytic results of the mass and species mass fractions of particles are given by [30]:

$$m(t) = m_{p0} - t(-r_\mathrm{B})\left(\frac{1}{2}\frac{\mathrm{M_D}}{\mathrm{M_B}} - 1\right) \tag{53}$$

$$X_\mathrm{B}(t) = \frac{m_{p0}X_{\mathrm{B0}} - (-r_\mathrm{B})t}{m_{p0} - t(-r_\mathrm{B})\left(\frac{1}{2}\frac{\mathrm{M_D}}{\mathrm{M_B}} - 1\right)} \tag{54}$$

$$X_\mathrm{D}(t) = \frac{m_{p0}X_{\mathrm{D0}} - (-r_\mathrm{D})t}{m_{p0} - t(-r_\mathrm{B})\left(\frac{1}{2}\frac{\mathrm{M_D}}{\mathrm{M_B}} - 1\right)} \tag{55}$$

$$X_\mathrm{I}(t) = \frac{m_{p0}X_{\mathrm{I0}}}{m_{p0} - t(-r_\mathrm{B})\left(\frac{1}{2}\frac{\mathrm{M_D}}{\mathrm{M_B}} - 1\right)} \tag{56}$$

Fig. 12(a) shows the numerical comparison of particle mass and relative error ($e = \frac{|m_p^a - m_p^s|}{m_p^a} \times 100\%$). The particle mass decreases and reaches a fixed value at about 1.5 s. The relative error is less than 0.0008 %. Fig. 12(b) and (c) illustrate species mass fraction and its absolute error. The mass fraction of reactant B decreases until zero at about 1.5 s while the mass fraction of product D increases. The mass of solid phase I is equal to the initial time while its mass fraction increases because of the decrease in particle mass. Notable, the absolute error ($e = |X^a - X^s|$) is used for comparison in Fig. 12(c) because the analytic solution of species mass fraction for species B goes to zero, leading to a division by zero. The absolute error of species mass fraction is less than 3×10^{-5}. Thus, the current model can accurately simulate the heterogeneous reaction.

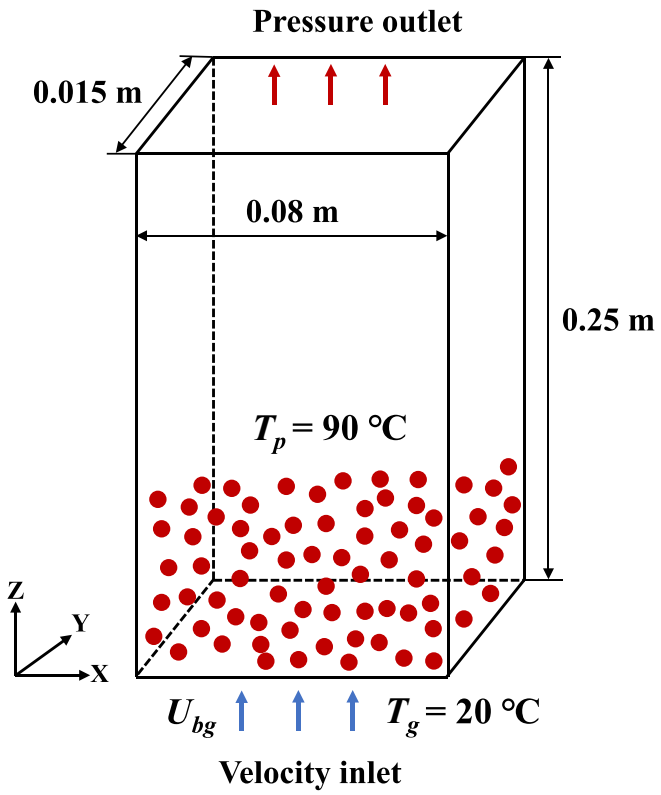

Fig. 13. Geometry configuration of the BFB.

4. Model validation and application

The assessment of the model's accuracy includes verification and validation. For the former, simulation results often compare with analytic solutions to illustrate the precision of the model. While for the model validation, the experimental results are chosen as the basis of comparison to illustrate the model's accuracy. In the previous section, the precision of the developed model has been detailed discussed. Thus, the accuracy of the developed model needs to be further validated. A lot of studies have been done to validate the accuracy of the current model in predicting the flow characteristics of gas–solid flow. Since this work focuses on the implementation of heat and mass transfer model, we only take the fully 3D spout-fluidized bed as an example to illustrate the flow validation, which can be found in Appendix A of the Supporting Information. Thus, in this section, the accuracy and reliability in numerically predicting the heat transfer and complex chemical reaction behavior are further validated in various experimental systems.

4.1. Heat transfer behavior in a BFB

The GPU-accelerated CFD-DEM reactive model is first validated by simulating the particle heat transfer process experimentally carried out by Patil et al. [49]. Fig. 13 presents the geometry configuration of the BFB, which is 0.08 m in width, 0.25 m in height, and 0.015 m in depth. The particles are 2500 kg/m^3 in density and 1.0 mm in diameter. Particles are initially packed at the lower part of the system and the initial temperature is 90 ℃. Based on the experimental setup, the total mass of particles is set as 75 g and 125 g, and the number of particles is 57,296 and 95,493, respectively. The fluidized gas is introduced from the

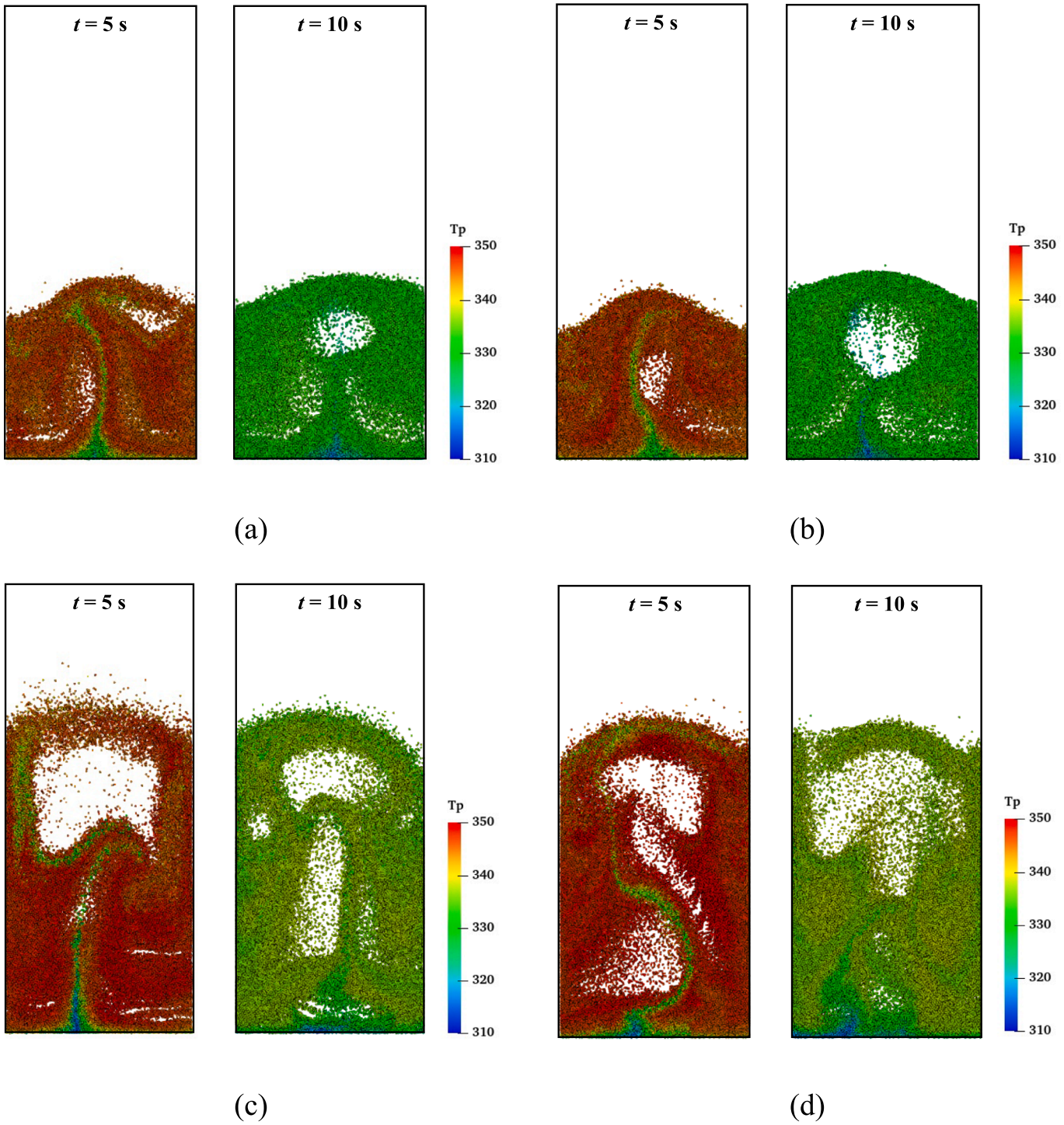

Fig. 14. Snapshots of solid motions and temperature distribution in BFB for $m = 75$ g (a, b) and $m = 125$ g (c, d); through GPU-accelerated CFD-DEM simulation (a, c) and CPU-based CFD-DEM simulation (b, d).

bottom and the superficial velocity is 1.54 m/s. The gas temperature is 20 ℃, thus the particles are cooled. Each simulation runs for 10 s and simulation parameters are detailed listed in Table S3 of the Supporting Information. To quantitatively validate the accuracy of the current model in simulating the heat transfer behavior, the mean particle temperature ($\overline{T}_p$) is calculated for comparison:

$$\overline{T}_p = \frac{1}{n}\sum_{i=1}^{n} T_{p,i} \tag{57}$$

where n is the total number of particles in the system.

Fig. 14 shows the particle temperature distribution in the BFB using both GPU-accelerated CFD-DEM and CPU-based CFD-DEM models. A similar distribution of particle temperature can be observed under two models. At 5 s and 10 s, a narrow cold particle zone can be observed at the center of the system. The generation of the cold zone may be caused by the cold fluidized gas introduced from the bottom. Thus, before moving upwards to the bed surface, the hot particles exchange more heat with cold gas. Fig. 15 shows the comparison of $\overline{T}_p$ between the

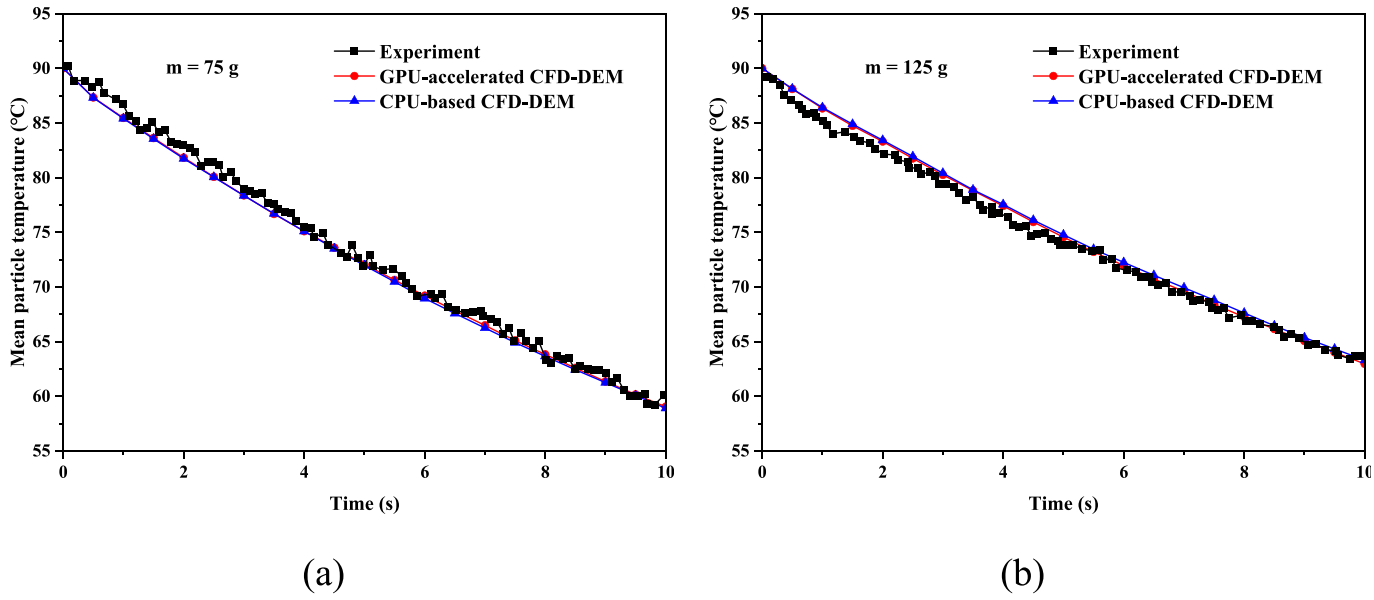

Fig. 15. Comparison of mean particle temperature between experimental data, GPU-accelerated CFD-DEM simulation results, and CPU-based CFD-DEM simulation results: (a) $m = 75$ g; (b) $m = 125$ g.

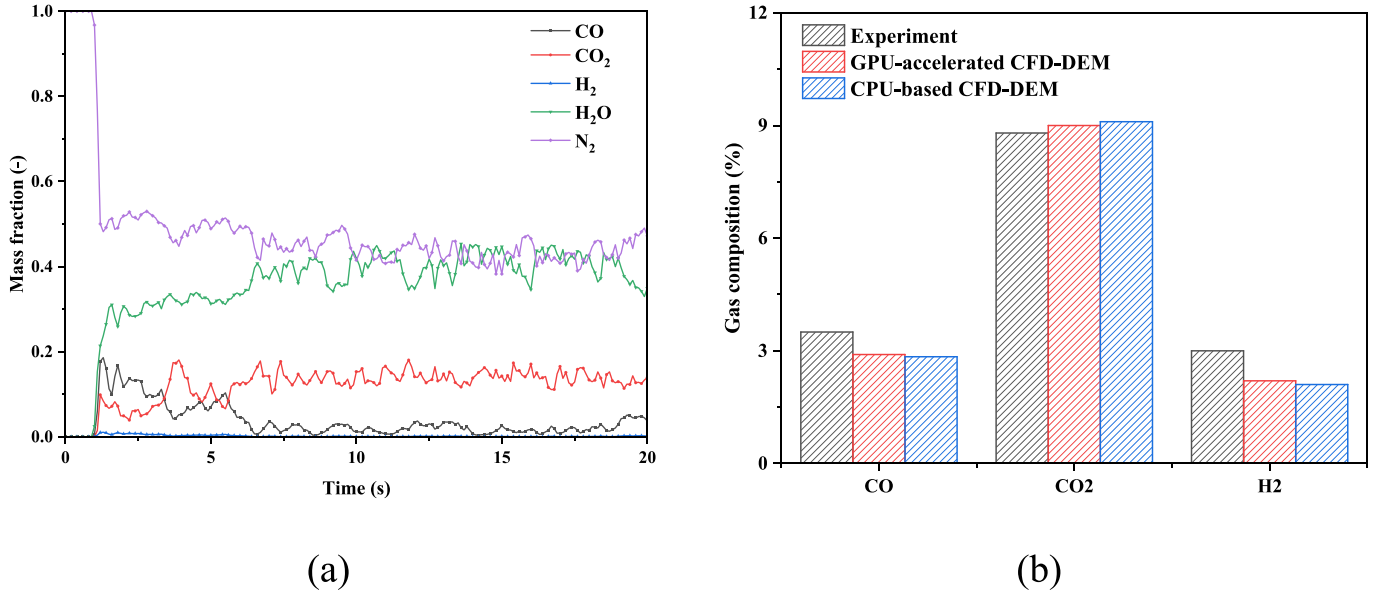

Fig. 16. (a) Variation of gas products at the outlet with time; (b) comparison of the gas composition at the outlet between experiment results, GPU-accelerated CFD-DEM simulation results, and CPU-based CFD-DEM simulation results.

experiment results and simulation results using both GPU-accelerated CFD-DEM and CPU-based CFD-DEM models. The $\overline{T}_p$ linearly reduces from 90 ℃ to about 60 ℃ at $t = 10$ s for the mass of 75 g, while about 65℃ for the mass of 125 g, respectively. The current GPU-accelerated CFD-DEM model can successfully capture the particle temperature under two conditions, which demonstrates the accuracy and reliability in numerically predicting the heat transfer behavior in the particle cooling process in a BFB.

4.2. Coal-fueled chemical looping gasification

The GPU-accelerated CFD-DEM reactive model is then applied to numerically study the coal-fueled chemical looping gasification (CLG) process experimentally studied by Chen et al. [50]. As presented in Fig. S4 of the Supporting Information, a quasi-3D CLG system is established referred to the experimental unit, which is 0.45 m in height and 0.038 m in width. The density of the oxygen carriers and coal particles are 3734 kg/m^3 and 1540 kg/m^3, respectively. The diameter of coal particles and oxygen carriers is the same which is 0.48 mm. The mass ratio of coal particles to oxygen carriers is 2.4: 100. The fluidized gas is introduced from the bottom at the superficial velocity of 0.24 m/s which is the mixture of H_2O/N_2 and the molar ratio is 1:1. The simulation case runs for 20 s and detailed operating parameters are listed in Table S4 of the Supporting Information.

The variation of gas products at the outlet with time is shown in Fig. 16(a). At about 1 s, the produced gas moves upwards and escapes from the outlet of the reactor. After about 7 s, the concentration of each type of gas species fluctuates around a constant value, which demonstrates that the chemical reactions reach the dynamics equilibrium state. Fig. 16(b) shows the comparison of the gas composition at the outlet

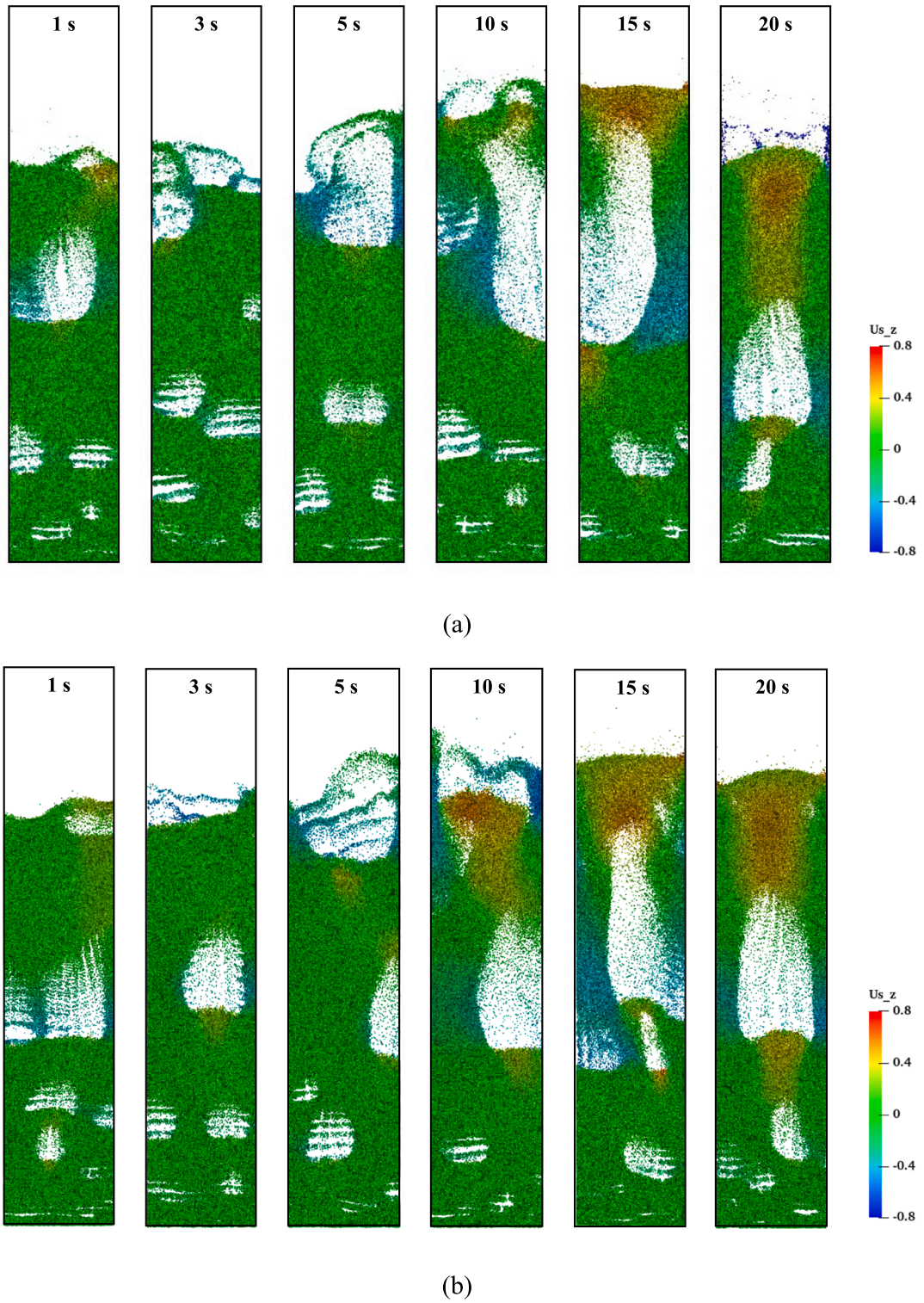

Fig. 17. Particle flow patterns in the reactor (colored by particle vertical velocity): GPU-accelerated CFD-DEM simulation (a) and CPU-based CFD-DEM simulation (b).

between the experiment results and simulation results using both GPU-accelerated CFD-DEM and CPU-based CFD-DEM models. The current GPU-accelerated CFD-DEM model successfully predicts the gas composition. The slight errors may be caused by the simplification of complex chemical reactions. Fig. 17 presents the variation of flow patterns with time using both GPU-accelerated CFD-DEM and CPU-based CFD-DEM models. In the lower part, small bubbles are generated because of the introduction of fluidized gas and coalesce into large bubbles and further rise until they burst near the bed surface. Fig. 18 shows the mass fraction distribution of gas species at $t = 20$ s using both GPU-accelerated CFD-DEM and CPU-based CFD-DEM models. The CO_2 is primarily produced in the upper region of the dense area due to the efficient mixing capabilities of particles. The distribution of H_2 and CO is similar, which is higher near the wall because of the higher concentration of char particles near the wall. Thus, the current model can accurately predict the thermochemical behavior in the coal-fueled CLG process.

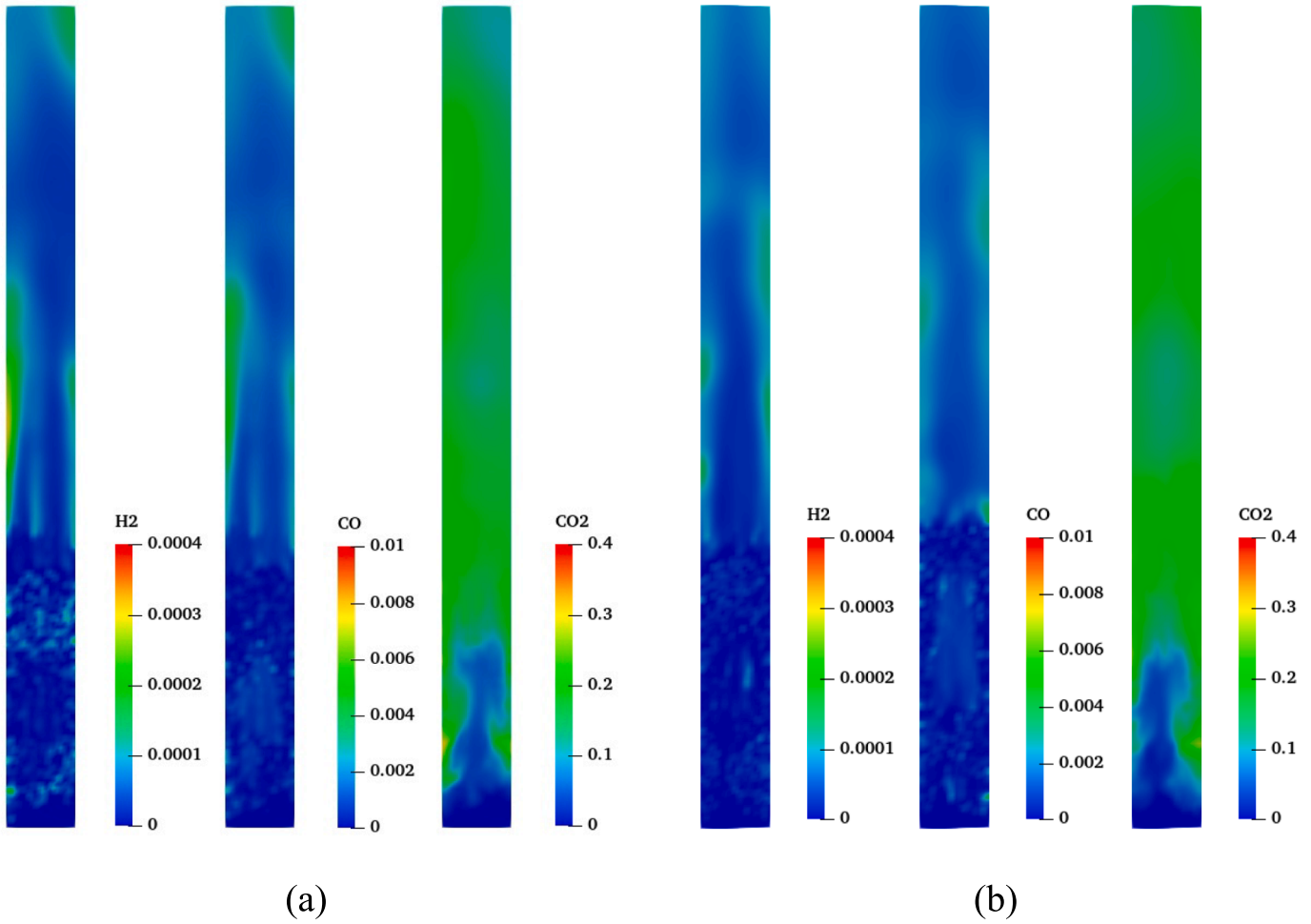

Fig. 18. Mass fraction distribution of gas species in the reactor at t = 20 s: GPU-accelerated CFD-DEM simulation (a) and CPU-based CFD-DEM simulation (b).

Table 2
The list of the main subroutines developed for the heat transfer and chemical reaction sub-models of the GPU-accelerated CFD-DEM reactive model.

Subroutine	Description
Thermo_cond	Calculate the particle conduction heat transfer rate.
Thermo_conv	Calculate the convection heat transfer rate.
Thermo_rad	Calculate the radiation heat transfer rate.
React_rates	Calculate the reaction heat transfer rate and interphase mass transfer based on the specific reaction kinetics.
Thermo_new	Update the temperature of particles.
React_new	Update the density, species composition, and mass of particles.

5. Speed-up performance

This section is to illustrate the speed-up performance of the GPU-accelerated heat transfer and chemical reaction sub-models. Table 2 lists the main subroutines developed for the heat transfer and chemical reaction sub-models of the GPU-accelerated CFD-DEM reactive model. Notably, the speed-up performance in this section is assessed through the coal-fueled CLG process validated in section 4.2, where the simulation details and analysis of results are provided. The speed-up ratio presented in Fig. 19 is calculated by comparing the simulation time of the GPU-accelerated model with the CPU-based model where 1 CPU core is used in the CPU simulation. The CPU-based CFD-DEM reactive model used in this section has been validated in our previous work and more details of this model can be found in Yu et al. [38]. Simulation cases are performed on a cluster with AMD EPYC 7H12 CPUs @ 2.6 GHz and NVIDIA A800 GPU. As shown in Fig. 19, the computational time can be greatly reduced through the GPU-accelerated method. The speed-up performance of the GPU-accelerated reactive model is highly relevant to the structure of code, thus different speed-up performances can be seen in Fig. 19. The highest speed-up ratio can achieve 289 for the react-new subroutine and the speed-up performance of other subroutines are also ideal. Fig. 20 shows the comparison of particle calculation time consumption under different calculated conditions. Due to the complex thermochemical behavior calculation, the traditional parallel algorithm using 8 or 16 CPU cores can obtain nearly 2 times or 4 times acceleration, respectively. Comparably, the GPU-accelerated reactive model can further accelerate the particle process, which can obtain nearly 6 times acceleration similar to using 32 CPU cores. Thus, the GPU-accelerated strategy is demonstrated to perform great speed-up performance and stability.

Table 3 details the GPU development and application in the last few years. Different methods and software are used to illustrate the acceleration performance of GPU-accelerated methods. It is noted that similar speed-up performance can be achieved using different models. However, these studies only focus on hydrodynamics without considering the thermochemical behavior, which limits its application in numerically studying dense gas–solid reacting systems. Considering the high cost of GPUs and the potential communication overhead between CPUs and GPUs, there is a need for additional improvements in the economic performance of CFD-DEM simulations. However, it should be noted that the GPU-accelerated CFD-DEM method offers practical advantages and can deliver better speed-up performance for users who have laptops

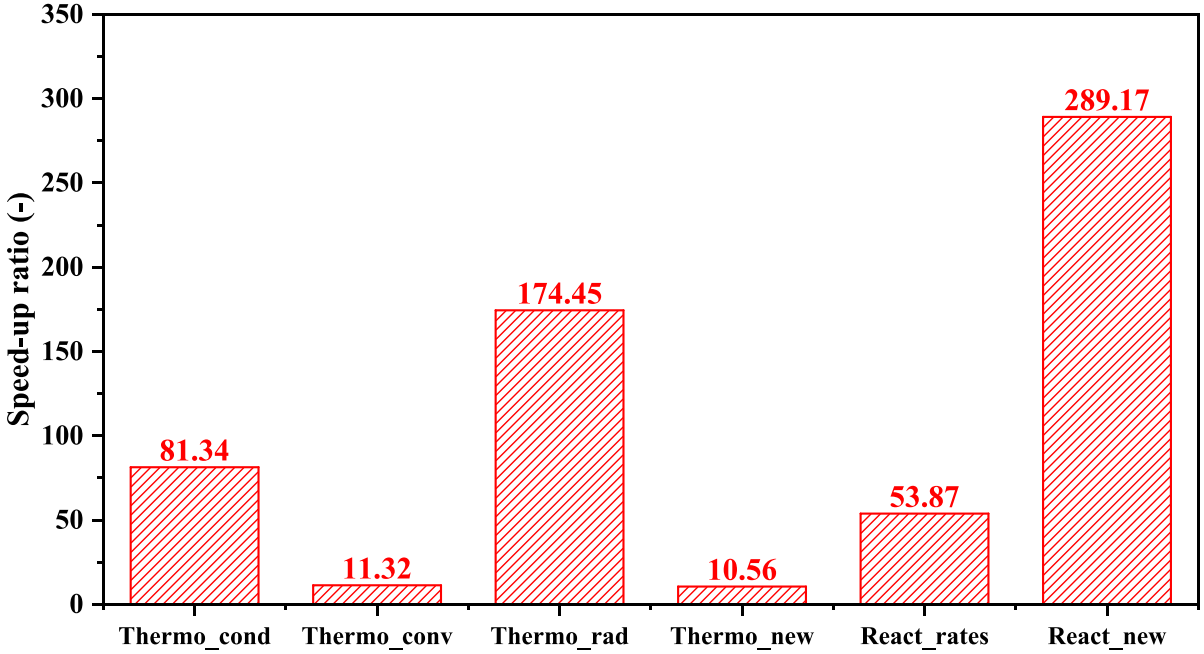

Fig. 19. Performance comparison of the main subroutines for the heat transfer and chemical reaction sub-models between the CPU-based CFD-DEM reactive method and the GPU-accelerated CFD-DEM reactive model.

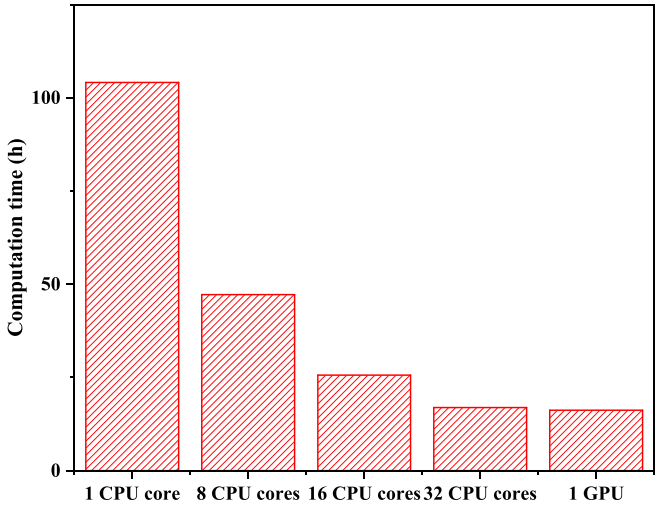

Fig. 20. Comparison of particle calculation time consumption under different calculated conditions.

equipped with a GPU card. This is particularly beneficial for those who require efficient simulation capabilities on portable computing devices. The GPU-accelerated method will be optimized even further, and the price of GPUs may decrease in the future. Consequently, the GPU-accelerated method shows great promise in simulating dense gas–solid reacting flow.

6. Conclusions

In this work, a GPU-accelerated CFD-DEM reactive model is developed, featuring heat transfer, homogenous reactions, and heterogeneous reactions. The accuracy, reliability, and acceleration performance of the developed model are examined under different conditions. Conclusions are summarized as follows:

Table 3
GPU development and application to dense particulate flow.

References	Model details	Device details	Computational details	Speed-up performance
He et al. (2020) [43]	ANSYS Fluent + Inhouse code HiPPs, CFD-DEM	Intel XEON E5-2650V4, NVIDIA Tesla P100	Large-scale fluidized bed with 1,327,104 particles	3.81 versus OpenMP and 6.31 times speedup versus MPI on 32 CPU cores
Tian et al. (2017) [51]	Inhouse code, GPU-based DEM	Intel XEON E5-2630, NVIDIA Tesla K80	Hopper flow with 8,000,000 particles	10.39 in 16 GPUs vs 128 CPU cores
Lu et al. (2022) [21]	MFiX, CFD-DEM	Intel XEON Gold 6148, NVIDIA Tesla P100	Particle packing process with 100,000 particles Bubbling fluidized bed with 1,320,000 particles	120–130 for DEM simulation 15 for CFD-DEM simulation
Gan et al. (2016) [52]	Inhouse code, GPU-based DEM	Intel XEON E5-2604, NVIDIA Tesla K20 M	Particle packing process with 300,000 particles	40–75, depending on the parallel algorithms used
Sousani et al. (2019) [53]	ANSYS Fluent + EDEM, CFD-DEM	NVIDIA Quadro GP100	Aggregate dryer demonstrating the fluid with 539,942 particles	6 for 1 GPU vs 30 CPUs for DEM 1.5 for 12 CPUs for CFD + 1 GPU for DEM vs 12 CPUs for CFD + 30 CPUs for DEM

1) In the GPU-accelerated CFD-DEM reactive model, the CPU and GPU can be coupled to complete the complex calculation, which is called heterogeneous computing. The code consists of the host code on the CPU and the device code on the GPU. The data on gas properties and

particle properties are stored in CPU memory and GPU memory, respectively. Through information communication, the CFD module and DEM module can be coupled to numerically study the dense gas–solid reacting flow.

2) The accuracy of the GPU-accelerated heat and mass transfer sub-models are detailly verified and simulation results are in line with analytic solutions. Additionally, this model can accurately capture the thermochemical behavior of the particle cooling process and the coal-fueled chemical looping gasification process, confirming its reliability in simulating dense gas–solid reacting systems.
3) The GPU-accelerated strategy is demonstrated to perform great speed-up performance. The highest speed-up ratio can achieve 289 for the react-new subroutine and the speed-up performance of other subroutines are also satisfactory. For the particle calculation, the GPU-accelerated reactive model can obtain nearly 6 times acceleration, which is faster than the traditional parallel algorithm using 8 or 16 CPU cores.

CRediT authorship contribution statement

Jiahui Yu: Writing – original draft, Validation, Software, Methodology. **Shuai Wang:** Writing – review & editing, Project administration. **Kun Luo:** Writing – review & editing, Project administration. **Jianren Fan:** Project administration.

Declaration of competing interest

The authors declare that they have no known competing financial interests or personal relationships that could have appeared to influence the work reported in this paper.

Data availability

The data that has been used is confidential.

Acknowledgments

We are grateful for the support from the National Natural Science Foundation of China (grant No. 51925603), the Fundamental Research Funds for the Central Universities (2022ZFJH004), and the Shanghai Pujiang Program (23PJ1412000).

Appendix A. Supplementary data

Supplementary data to this article can be found online at https://doi.org/10.1016/j.cej.2024.149480.

References

[1] S. Banerjee, R. Agarwal, Transient reacting flow simulation of spouted fluidized bed for coal-direct chemical looping combustion with different fe-based oxygen carriers, Appl. Energy. 160 (2015) 552–560.
[2] H. Boujjat, S. Rodat, S. Chuayboon, S. Abanades, Numerical simulation of reactive gas-particle flow in a solar jet spouted bed reactor for continuous biomass gasification, Int. J. Heat Mass Transf. 144 (2019) 118572.
[3] R. Jovanovic, A. Milewska, B. Swiatkowski, A. Goanta, H. Spliethoff, Numerical investigation of influence of homogeneous/heterogeneous ignition/combustion mechanisms on ignition point position during pulverized coal combustion in oxygen enriched and recycled flue gases atmosphere, Int. J. Heat Mass Transf. 54 (2011) 921–931.
[4] S. Natsui, H. Takai, R. Nashimoto, T. Kikuchi, R.O. Suzuki, Model study of the effect of particles structure on the heat and mass transfer through the packed bed in ironmaking blast furnace, Int. J. Heat Mass Transf. 91 (2015) 1176–1186.
[5] H. Zheng, X. Liu, Y. Xuan, Y. Ding, G. Flamant, Efficient direct solar-driven thermochemical energy storage of (almgfemn) oxcaco3 pellets in a fluidized bed reactor, Energy Convers. Manage. (2023).
[6] S. Wang, C. Hu, K. Luo, J. Yu, J. Fan, Multi-scale numerical simulation of fluidized beds: model applicability assessment, Particuology. 80 (2023) 11–41.
[7] S. Wang, Y. Shen, Coarse-grained cfd-dem modelling of dense gas-solid reacting flow, Int. J. Heat Mass Transf. 184 (2022) 122302, https://doi.org/10.1016/j.ijheatmasstransfer.2021.122302.
[8] W. Zhong, A. Yu, G. Zhou, J. Xie, H. Zhang, Cfd simulation of dense particulate reaction system: approaches, recent advances and applications, Chem. Eng. Sci. 140 (2016) 16–43.
[9] J. Yu, S. Wang, K. Luo, D. Li, J. Fan, Study of biomass gasification in an industrial-scale dual circulating fluidized bed (dcfb) using the eulerian-lagrangian method, Particuology. 83 (2023) 156–168.
[10] A.M. Mauerhofer, J.C. Schmid, F. Benedikt, J. Fuchs, S. Müller, H. Hofbauer, Dual fluidized bed steam gasification: change of product gas quality along the reactor height, Energy. 173 (2019) 1256–1272.
[11] C. Loha, P.K. Chatterjee, H. Chattopadhyay, Performance of fluidized bed steam gasification of biomass-modeling and experiment, Energy Conv. Manag. 52 (2011) 1583–1588.
[12] R.B. Bates, A.F. Ghoniem, W.S. Jablonski, D.L. Carpenter, C. Altantzis, A. Garg, J. L. Barton, R. Chen, R.P. Field, Steam-air blown bubbling fluidized bed biomass gasification (bfbbg): multi-scale models and experimental validation, Aiche J. 63 (2017) 1543–1565.
[13] Y. Du, L. Zhang, A.S. Berrouk, Exergy analysis of propane dehydrogenation in a fluidized bed reactor: experiment and mp-pic simulation, Energy Conv. Manag. 202 (2019) 112213.
[14] F. Alobaid, N. Almohammed, M.M. Farid, J. May, P. Rößger, A. Richter, B. Epple, Progress in cfd simulations of fluidized beds for chemical and energy process engineering, Prog. Energy Combust. Sci. 91 (2022) 100930.
[15] J. Lin, K. Luo, L. Sun, S. Wang, C. Hu, J. Fan, Numerical investigation of nickel-copper oxygen carriers in chemical-looping combustion process with zero emission of co and h2, Energy Fuels 33 (2019) 12096–12105.
[16] Z. Li, H. Xu, W. Yang, S. Wu, Numerical study on the effective utilization of high sulfur petroleum coke for syngas production via chemical looping gasification, Energy. 235 (2021) 121395.
[17] S. Wang, Y. Shen, Particle-scale study of heat and mass transfer in a bubbling fluidised bed, Chem. Eng. Sci. 240 (2021) 116655.
[18] D. Kong, K. Luo, S. Wang, J. Yu, J. Fan, Particle behaviours of biomass gasification in a bubbling fluidized bed, Chem. Eng. J. 428 (2022) 131847.
[19] S. Wang, Y. Shen, Cfd-dem modelling of raceway dynamics and coke combustion in an ironmaking blast furnace, Fuel. 302 (2021) 121167.
[20] C. Wu, Y. Cheng, Y. Ding, Y. Jin, Cfd-dem simulation of gas-solid reacting flows in fluid catalytic cracking (fcc) process, Chem. Eng. Sci. 65 (2010) 542–549.
[21] L. Lu, Gpu accelerated mfix-dem simulations of granular and multiphase flows, Particuology. 62 (2022) 14–24.
[22] H.R. Norouzi, R. Zarghami, N. Mostoufi, New hybrid cpu-gpu solver for cfd-dem simulation of fluidized beds, Powder Technol. 316 (2017) 233–244.
[23] S. Wang, Y. Shen, Cfd-dem study of biomass gasification in a fluidized bed reactor: effects of key operating parameters, Renew. Energy. 159 (2020) 1146–1164, https://doi.org/10.1016/j.renene.2020.06.001.
[24] R. Garg, J. Galvin, T. Li, S. Pannala, Open-source mfix-dem software for gas–solids flows: part i—verification studies, Powder Technol. 220 (2012) 122–137, https://doi.org/10.1016/j.powtec.2011.09.019.
[25] P.A. Cundall, O.D. Strack, A discrete numerical model for granular assemblies, Géotechnique. 29 (1979) 47–65.
[26] S. Wang, K. Luo, J. Fan, Cfd-dem coupled with thermochemical sub-models for biomass gasification: validation and sensitivity analysis, Chem. Eng. Sci. 217 (2020) 115550, https://doi.org/10.1016/j.ces.2020.115550.
[27] D. Gidaspow, Multiphase flow and fluidization: continuum and kinetic theory description, J. Non-Newton. Fluid Mech. 55 (1994) 207–208.
[28] J. Li, D.J. Mason, A computational investigation of transient heat transfer in pneumatic transport of granular particles, Powder Technol. 112 (2000) 273–282.
[29] G.K. Batchelor, R.W. O'Brien, Thermal or electrical conduction through a granular material, Proc. R. Soc. London. A. Mathem. Phys. Sci., 355 (1977) 313–333.
[30] J.M. Musser, Modeling of Heat Transfer and Reactive Chemistry for Particles in Gas-Solid Flow Utilizing Continuum-Discrete Methodology (cdm), West Virginia University, 2011.
[31] Z.Y. Zhou, A.B. Yu, P. Zulli, Particle scale study of heat transfer in packed and bubbling fluidized beds, Aiche J. 55 (2009) 868–884.
[32] J. Bruchmüller, K.H. Luo, B. Van Wachem, Tar formation variations during fluidised bed pyrolytic biomass conversion, Proc. Combust. Inst. 34 (2013) 2373–2381.
[33] C. Fan, H. Jin, Numerical simulation of gasification of a shrinking char particle in supercritical water, Fuel. 318 (2022) 123692.
[34] A. Gómez-Barea, B. Leckner, Modeling of biomass gasification in fluidized bed, Prog. Energy Combust. Sci. 36 (2010) 444–509.
[35] X. Ku, T. Li, T. Løvås, Cfd-dem simulation of biomass gasification with steam in a fluidized bed reactor, Chem. Eng. Sci. 122 (2015) 270–283.
[36] H.R. Norouzi, R. Zarghami, R. Sotudeh-Gharebagh, N. Mostoufi, Coupled CFD-DEM Modeling: Formulation, Implementation and Application to Multiphase Flows, John Wiley & Sons, 2016.
[37] Z. Peng, E. Doroodchi, C. Luo, B. Moghtaderi, Influence of void fraction calculation on fidelity of cfd-dem simulation of gas-solid bubbling fluidized beds, Aiche J. 60 (2014) 2000–2018.
[38] J. Yu, S. Wang, D. Kong, K. Luo, J. Fan, Coal-fueled chemical looping gasification: a cfd-dem study, Fuel 345 (2023) 128119.
[39] R.C. Everson, H.W.J.P. Neomagus, H. Kasaini, D. Njapha, Reaction kinetics of pulverized coal-chars derived from inertinite-rich coal discards: characterisation and combustion, Fuel 85 (2006) 1067–1075, https://doi.org/10.1016/j.fuel.2005.10.025.
[40] K. Mahalatkar, J. Kuhlman, E.D. Huckaby, T. O'Brien, Cfd simulation of a chemical-looping fuel reactor utilizing solid fuel, Chem. Eng. Sci. 66 (2011) 3617–3627, https://doi.org/10.1016/j.ces.2011.04.025.

[41] M. Su, H. Zhao, J. Ma, Computational fluid dynamics simulation for chemical looping combustion of coal in a dual circulation fluidized bed, Energy Conv. Manag. 105 (2015) 1–12, https://doi.org/10.1016/j.enconman.2015.07.042.
[42] S. Wang, W. Yin, Z. Li, X. Yang, K. Zhang, Numerical investigation of chemical looping gasification process using solid fuels for syngas production, Energy Conv. Manag. 173 (2018) 296–302, https://doi.org/10.1016/j.enconman.2018.07.043.
[43] Y. He, F. Muller, A. Hassanpour, A.E. Bayly, A cpu-gpu cross-platform coupled cfd-dem approach for complex particle-fluid flows, Chem. Eng. Sci. 223 (2020) 115712.
[44] S.V. Patankar, D.B. Spalding, A calculation procedure for heat, mass and momentum transfer in three-dimensional parabolic flows, Numerical Prediction of Flow, Heat Transfer, Turbulence and Combustion 1983 54–73.
[45] D.H.M.A. Van, S.A.M. Van, N.G. Deen, J.A.M. Kuipers, Numerical simulation of dense gas-solid fluidized beds: a multiscale modeling strategy, Annu. Rev. Fluid Mech. 40 (2008) 47–70.
[46] C.L. Wu, O. Ayeni, A.S. Berrouk, K. Nandakumar, Parallel algorithms for cfd-dem modeling of dense particulate flows, Chem. Eng. Sci. 118 (2014) 221–244.
[47] J.H. Ferziger, M. Peric, A. Leonard, Computational methods for fluid dynamics, Phys. Today. 50 (1997) 80–84.
[48] Y. Tsuji, T. Kawaguchi, T. Tanaka, Discrete particle simulation of two-dimensional fluidized bed, Powder Technol. 77 (1993) 79–87.
[49] A.V. Patil, E. Peters, V.S. Sutkar, N.G. Deen, J. Kuipers, A study of heat transfer in fluidized beds using an integrated dia/piv/ir technique, Chem. Eng. J. (2015).
[50] L. Chen, L. Yang, F. Liu, H.S. Nikolic, Z. Fan, K. Liu, Evaluation of multi-functional iron-based carrier from bauxite residual for h2-rich syngas production via chemical-looping gasification, Fuel Process. Technol. 156 (2017) 185–194, https://doi.org/10.1016/j.fuproc.2016.10.030.
[51] Y. Tian, S. Zhang, P. Lin, Q. Yang, G. Yang, L. Yang, Implementing discrete element method for large-scale simulation of particles on multiple gpus, Comput. Chem. Eng. 104 (2017) 231–240.
[52] J.Q. Gan, Z.Y. Zhou, A.B. Yu, A gpu-based dem approach for modelling of particulate systems, Powder Technol. 301 (2016) 1172–1182.
[53] M. Sousani, A.M. Hobbs, A. Anderson, R. Wood, Accelerated heat transfer simulations using coupled dem and cfd, Powder Technol. 357 (2019) 367–376.